Nano Research
2019, 12(6): 1279–1292

ISSN 1998-0124 CN 11-5974/O4
https://doi.org/10.1007/s12274-019-2343-6

Review Article

Recent progress in engineering near-infrared persistent luminescence nanoprobes for time-resolved biosensing/bioimaging

Ling Liang[1,§], Na Chen[1,§], Yiyi Jia[1], Qinqin Ma[2], Jie Wang[2], Quan Yuan[1,2] (✉), and Weihong Tan[1]

[1] *Molecular Science and Biomedicine Laboratory, Institute of Chemical Biology and Nanomedicine, College of Chemistry and Chemical Engineering, Hunan University, Changsha 410082, China*

[2] *Key Laboratory of Analytical Chemistry for Biology and Medicine (Ministry of Education), College of Chemistry and Molecular Sciences, Wuhan University, Wuhan 430072, China*

[§] *Ling Liang and Na Chen contributed equally to this work.*

Received: 11 December 2018 / **Revised:** 12 February 2019 / **Accepted:** 15 February 2019

ABSTRACT

Persistent luminescence nanoprobes (PLNPs) can remain luminescent after ceasing excitation. Due to the ultra-long decay time of persistent luminescence (PersL), autofluorescence interference can be efficiently eliminated by collecting PersL signal after autofluorescence decays completely, thus the imaging contrast and sensing sensitivity can be significantly improved. Since near-infrared (NIR) light shows reduced scattering and absorption coefficient in penetrating biological organs or tissues, near-infrared persistent luminescence nanoprobes (NIR PLNPs) possess deep tissue penetration and offer a bright prospect in the areas of *in vivo* biosensing/bioimaging. In this review, we firstly summarize the design of different types of NIR PLNPs for biosensing/bioimaging, such as transition metal ions-doped NIR PLNPs, lanthanide ions-doped NIR PLNPs, organic molecules-based NIR PLNPs, and semiconducting polymer self-assembled NIR PLNPs. Notably, organic molecules-based NIR PLNPs and semiconductor self-assembled NIR PLNPs, for the first time, were introduced to the review of PLNPs. Secondly, the effects of different types of charge carriers on NIR PersL and luminescence decay of NIR PLNPs are significantly emphasized so as to build up an in-depth understanding of their luminescence mechanism. It includes the regulation of valence band and conduction band of different host materials, alteration of defect types, depth and concentration changes caused by ion doping, effective radiation transitions and energy transfer generated by different luminescence centers. Given the design and potential of NIR PLNPs as long-lived luminescent materials, the current challenges and future perspective in this rapidly growing field are also discussed.

KEYWORDS

near-infrared, persistent luminescence nanoprobes, biosensing, bioimaging

1 Introduction

Under ultraviolet (UV) or visible light irradiation, some materials absorb excitation energy and release it as a differently colored light either in a fast fluorescent form or in a slow form of phosphorescence or long persistent luminescence (PersL) [1]. Utilizing fluorophores with lifetimes in the same order of nanoseconds as the background signal, it is extremely difficult to decode molecular and cellular behaviors in complex biological environments, especially in the analysis of molecular information in biological tissues [2, 3]. In response to this, time-resolved photoluminescence technology that is capable to effectively distinguish the substances with different luminescence lifetimes/luminescence decay has been developed to eliminate the background signal [4–6]. The time-resolved photoluminescence technology possesses many advantages in biosensing and bioimaging. Firstly, the luminescence lifetime is hardly affected by concentration variation of intracellular luminescent probes or excitation laser power [7, 8]. Secondly, it is well known that the maximum lifetime of biological autofluorescence is about 10 ns [9], whereas the long-lived luminescent probe can remain luminescent for several minutes or even hours after cessation of the excitation [10, 11]. Collecting the long-lived luminescent signal after short-lived signals fade can selectively separate the probe signal from the biological autofluorescence [12]. Thus, based on the different emission attenuation rates between the biological sample and the long-lived luminescent probe, short-lived unwanted noise can be eliminated by time-gated luminescence signal measurement, considerably improving the signal-to-noise ratio and detection accuracy.

With slower light release processes, long-lived luminescent probes, including lanthanides [13], transition-metal complexes [14], inorganic nanomaterials [15], and metal clusters [16], have been used for time-resolved biosensing/bioimaging. Persistent luminescence materials as long-lived luminescent imaging reagents have also been reported almost 20 years ago, whose PersL can last for hours or even days after the stoppage of excitation. Largely inspired by $SrAl_2O_4:Eu^{2+},Dy^{3+}$ with the luminescence lifetime longer than 30 h proposed by in 1996, persistent luminescence materials have been rapidly developed [11, 17]. Since then, many inorganic materials composed of host materials and activators were discovered to exhibit PersL. The reported host materials include germinates [18], gallate [19], silicates [20], aluminates [21], stannates [22], sulfides [23], phosphates [24] and titanates [25]; activators [26–30] include transition metal ions (Mn^{2+} or Cr^{3+}) [29, 31–34] and lanthanide ions (Eu^{2+}, Yb^{3+}, Ce^{3+} or Pr^{3+}) [24, 35–37]. These materials as persistent luminescence nanoprobes (PLNPs) opened a new door to the biological applications from biosensing/bioimaging to theranostics.

Address correspondence to yuanquan@whu.edu.cn

Signal acquisition of PLNPs was performed after external excitation is turned off, thereby completely eliminating autofluorescence and significantly improving the signal-to-noise ratio and sensitivity [38]. Moreover, on account of the long PersL of these nanoparticles lasting for a long time (even to several days), long-term tracking for *in vivo* real-time biosensing/bioimaging can be achieved after injection.

Normally, the emission wavelength of PLNPs has been extended from UV to near-infrared (NIR) light [39–42]. Considering the limited penetration depth of visible light, there has been increasing interest in employing near-infrared persistent luminescent nanoprobes (NIR PLNPs) to obtain high-quality time-resolved photoluminescence images of biological samples with minimized autofluorescence interference [43–46]. The PersL of NIR PLNPs falls within the tissue transparency window varying from 650 to 1,800 nm [47–49], which have stronger signal-to-noise ratio and deeper tissue penetration due to the reduced scattering and minimal absorption coefficient of NIR light transmitted through biological organs or tissues. However, the review about the summary of NIR PLNPs is lacking. At present, a number of excellent reviews emphasize the synthesis, chemical engineering of PLNPs and their biological applications. Qiu et al. presented a very comprehensive summary about the synthetic methods, luminescence mechanisms, characterization techniques, materials system, and the applications of persistent phosphors [50]. Richard et al. systematically summarized the achievements persistent luminescence nanoparticles with different matrixes for *in vitro* and *in vivo* imaging applications [51]. Yan et al. highlighted the advances in fabricating specific PLNPs-based nanoprobes and their biological applications from biosensing/bioimaging to theranostics [52]. Wang et al. summarized the preparation of PLNPs and the applications of PLNPs in biosensing, bioimaging and cancer therapy [53]. Singh et al. presented an overview of metal ions-doped red and NIR persistent materials and their applications for bioimaging [54]. These reviews mainly focus on PLNPs and their synthetic methods, surface engineering and biological applications. In this review, we firstly summarize the design and applications of various kinds of NIR PLNPs, including transition metal ions-doped NIR PLNPs, lanthanide ions-doped NIR PLNPs, organic molecules-based NIR PLNPs, and semiconducting polymer self-assembled NIR PLNPs. Secondly, the effects of different types of charge carriers on NIR PersL and luminescence decay of NIR PLNPs are significantly emphasized so as to build up an in-depth understanding of their luminescence mechanism. It includes the regulation of valence band and conduction band of different host materials, alteration of defect types, depth and concentration changes caused by ion doping, effective radiation transitions and energy transfer generated by different luminescence centers, etc. Finally, the review discusses the remaining challenges and future research directions in this field.

2 Transition metal ions-doped NIR PLNPs

There are two types of active centers in long persistent luminescence materials: emitters and traps. Emitters as the radiation centers can be emitted after excitation, whereas traps usually store excitation energy. Due to thermal or other physical stimulations, the excitation energy is gradually released to the emitters following by producing radiative transition. The emission wavelength of the persistent luminescence materials is primarily determined by emitters, while the PersL intensity and luminescence decay are dominated by trapping states associated with lattice defects or co-dopants. When it comes to the trap properties of a given persistent luminescence materials, there is no standard to describe it. Usually, three main features should be considered, such as trap types, concentrations and depths. For traps [55], the trap concentrations can be confirmed by a positron annihilation lifetime spectroscopy (PALS) after verifying the types [56], whereas the trap depth is necessarily analyzed by the thermal luminescence (TL) curves, which act a pivotal part in determining the luminescence decay [57]. As a consequence, to engineer NIR PLNPs for time-resolved biosensing/bioimaging, a proper emitter for emitting NIR light and a suitable host capable of generating appropriate traps are required to be seriously considered.

2.1 Cr^{3+}-doped NIR PLNPs

Cr^{3+} is a highly desirable NIR emitter since its $3d^3$ electron configuration produces a narrow-band emission close to 700 nm attributed to the spin-forbidden $^2E \rightarrow {}^4A_2$ transition, and a broadband emission (650–1,000 nm) ascribed to the spin-allowed $^4T_2 \rightarrow {}^4A_2$ transition. Cr^{3+}-doped $ZnGa_2O_4$ spinel material, one of the most prominent materials, is of great interest in NIR PersL. The $ZnGa_2O_4$ crystal has a cubic AB_2O_4 spinel structure crystallizing in the $Fd\bar{3}m$ (O_h^7) space group, in which Zn^{2+}, Ga^{3+} ions occupy the tetrahedral A-sites and the octahedral B-sites, respectively [58–60]. The doped Cr^{3+} preferentially occupy the crystalline Ga^{3+} site in view of their identical valence and identical ionic radius (0.615 Å vs. 0.62 Å) [61] in distorted octahedral coordination, which gives rise to a strong NIR PersL at 696 nm [62–64].

In 1973, van Gorkom et al. investigated the emission spectra of Cr^{3+} pairs in the spinel $ZnGa_2O_4$ in detail [65]. The authors described the excited state of the pair by introducing a modified exchange Hamiltonian to explain the optical absorption and emission spectra of $ZnGa_2O_4$:Cr^{3+}, and proposed an energy-level scheme for Cr^{3+} in $ZnGa_2O_4$:Cr^{3+} bulk crystals. Afterwards, Roy et al. first reported that nanocrystalline $ZnGa_2O_4$:Cr^{3+} shows a broad luminescence between 600 and 800 nm along with sharp spectral transition lines of Cr^{3+} [63]. The authors analyzed the exchange interaction between the $ZnGa_2O_4$ host and Cr^{3+} dopant ion from crystal field theory. The electronic band structure of nanocrystalline $ZnGa_2O_4$ has the significant effect on intensity of emission. Later, Bessiere' group investigated the NIR PersL mechanism of $ZnGa_2O_4$:Cr^{3+} by varying the nominal Zn/Ga stoichiometry and verified that Cr^{3+} distorted by a neighboring antisite defect as a recombination centre result in NIR PersL, rather than ideal Cr^{3+}. $ZnGa_2O_4$:Cr^{3+} was selected as a new high-performance NIR PLNPs for *in vivo* imaging for the first time as it corresponds to a transmission maximum for the biological tissues [59].

To satisfy the crucial demand for ultrasensitive biodetection and/or long-term bioimaging, the synthesis of high-quality PLNPs with bright NIR PersL and long luminescence decay time is also an urgent to consider. Many reported PLNPs were synthesized through high-temperature calcination followed by a physical grinding process. The prepared nanoparticles based on the "top-down" strategy usually aggregate with a poor size distribution and also sacrifice the PersL properties. In contrast, the "bottom-up" hydro/solvothermal strategy for the preparation of PLNPs shows the unique advantages of controllable size, uniform shape and effective surface functionalization [19, 66–69], which will be more promising in terms of *in vivo* biosensing/bioimaging. The most successful example for hydrothermal synthesis of NIR PLNPs was demonstrated by Maldiney and co-workers. The author synthesized $ZnGa_2O_4$:Cr^{3+} with size of 50–100 nm by hydrothermal method, which method is dependent on the pH value, initial composition, reaction time and reaction temperature. Such unprecedented NIR PersL characteristics of Cr^{3+}-doped NIR PLNPs completely avoid tissue autofluorescence and open alternatives to high-sensitivity *in vivo* optical detection, long-term bioimaging in living animals (Fig. 1(a)) [6]. Another successful example for the hydrothermal synthesis of monodisperse sub-10 nm $ZnGa_2O_4$:Cr^{3+} PLNPs was demonstrated by Han et al. in 2015 [19]. The Cr^{3+}-doped NIR PLNPs can be directly synthesized in aqueous solution by a solid-state-reaction-free chemical method. Such monodisperse attributes are premises for the further surface functionalization and beneficial to the *in vivo* colloidal stability and

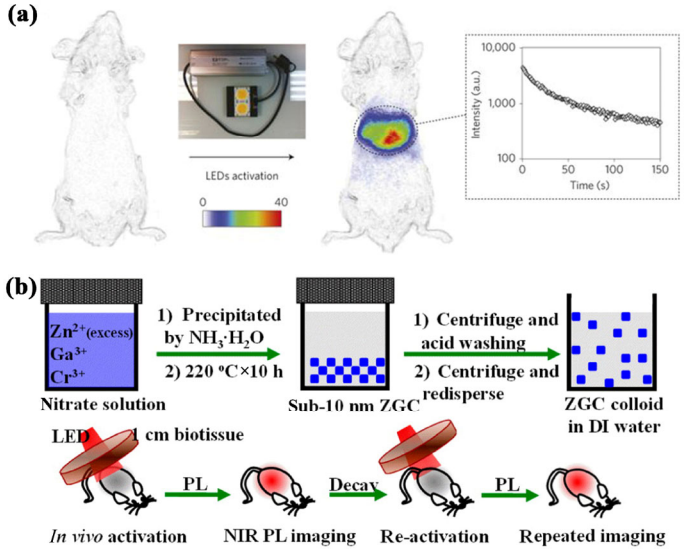

Figure 1 (a) *In vivo* imaging with $ZnGa_2O_4:Cr^{3+}$ PLNPs after LED activation. The inset shows a luminescence decay curve corresponding to the NIR PersL signal. Reproduced with permission from Ref. [6], © Nature Publishing Group 2014. (b) Schematic illustration of the synthesis and *in vivo* deep-tissue imaging of $ZnGa_2O_4:Cr^{3+}$ PLNPs. Reproduced with permission from Ref. [19], © American Chemical Society 2015.

biodistribution of NIR PLNPs ((Fig. 1(b)). A step further, Chen et al. designed a facile strategy for the synthesis of monodisperse, rechargeable and light emitting diode (LED)-activated $ZnGa_2O_4:Cr^{3+}$ NIR PLNPs through a modified solvothermal liquid–solid-solution method [64]. High-quality $ZnGa_2O_4:Cr^{3+}$ PLNPs are roughly spherical and show a broad emission band with a sharp peak centered at 695 nm (Figs. 2(a) and 2(b)). The luminescence decay more than 2 h was detected under UV excitation, ascribed to the direct quantum tunneling process between the deep traps and the ^2E or $^4T_2$ (t_2^2e) state of Cr^{3+}. By utilizing their unique NIR PersL, biotinylated NIR PLNPs as sensitive and specific luminescent nanoprobes exhibited a low detection limit (~ 150 pM) in a heterogeneous bioassay of the avidin protein (Fig. 2(c)), thereby revealing the great potential of these NIR PLNPs in ultrasensitive biodetection and bioimaging. As already mentioned, Cr^{3+} ion has two excited levels, ^2E and $^4T_2(^4F)$, which are sensitive to their external surrounding. Since a thermal equilibrium exists between ^2E and $^4T_2(^4F)$ [70], the contributions of radiative transitions from $^2E \rightarrow {}^4A_2$ and $^4T_2 \rightarrow {}^4A_2$ of both surface and interior Cr^{3+} ions to external surroundings and NIR luminescence can be distinguished. Zhang et al. designed a bifunctional ratiometric PersL nanothermometer with $ZnGaGeO_4:Cr^{3+}$ for simultaneous *in vivo* bioimaging and local tissue temperature sensing in the physiological temperature range (298–325 K) (Fig. 2(d)) [71]. Above all, such Cr^{3+}-doped NIR PLNPs with multifold functions broad the feasibility in modern biomedicine sensing and imaging.

Inspired by the Cr^{3+}-activated gallate for NIR PersL, Pan et al. realized NIR PersL in $La_3Ga_5GeO_{14}:Cr^{3+}$ phosphor, whose luminescence decay time is more than 1 h [72]. For the practical biomedical applications of NIR PLNPs, the lack of controllable size or luminescence decay for NIR PersL inevitably imposes significant limitations. Therefore, it is highly desirable to develop NIR PLNPs with tunable properties. To attain the longer PersL, the same group also prepared a series of Cr^{3+}-doped zinc gallogermanate NIR PLNPs, achieving a super-long NIR luminescence decay of more than 360 h. The electron trapping and detrapping recombination processes in $Zn_3Ga_2Ge_2O_{10}:Cr^{3+}$ was proposed, which were related to the optical transitions and electron transfer processes through either conduction band or energy-matched tunnelling channels [73]. Additionally, our group demonstrated that zinc gallogermanate ($Zn_{1+x}Ga_{2-2x}Ge_xO_4$:Cr, $0 \le x \le 0.5$, ZGGO:Cr) with composition-dependent size and NIR PersL can be directly synthesized to effectively meet different practical biomedical requirements [74]. With the increase of x in the chemical formula, the size, intensity and decay time of NIR PersL in ZGGO:Cr nanoparticles can be fine-tuned (Figs. 3(a)–3(c)). What is more, the size of the ZGGO:Cr nanoparticles gradually increases by simply changing x in the formula. For *in vivo* imaging, ZGGO:Cr nanoparticles can efficiently eliminate tissue autofluorescence by collecting the NIR PersL signal of ZGGO:Cr nanoparticles after the short-lived autofluorescence decays completely (Figs. 3(d) and 3(e)). To conclude, the developed ZGGO:Cr nanoparticles give tremendous opportunities for autofluorescence-free bioimaging and can further contribute to potential areas, such as real-time monitoring of biological processes and constructing guiding systems for surgery.

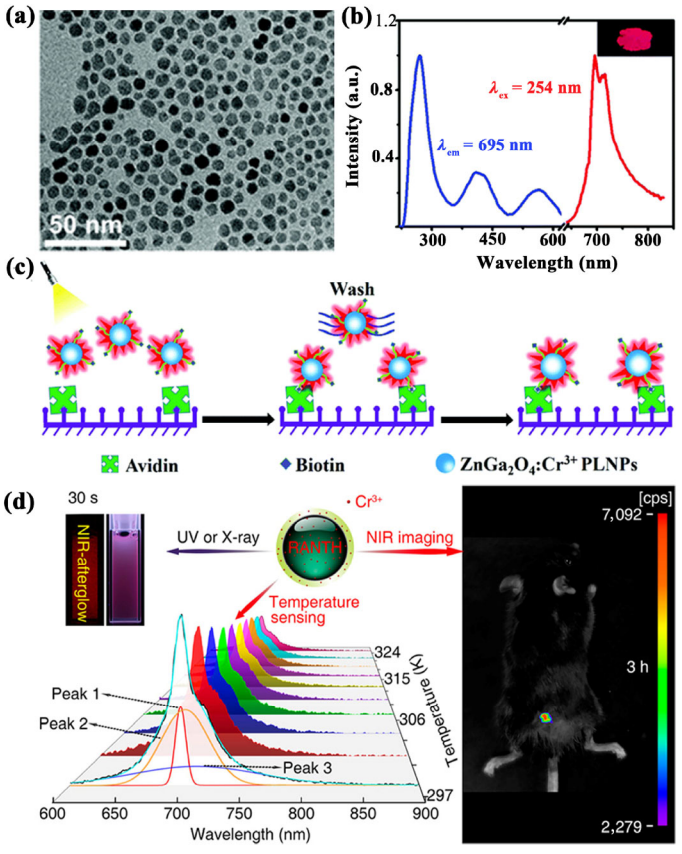

Figure 2 (a) TEM image of $ZnGa_2O_4$:0.4% Cr^{3+} PLNPs. (b) Excitation (blue curve) and emission (red curve) spectra of $ZnGa_2O_4$:0.4% Cr^{3+} PLNPs at room temperature. The inset is digital photo of the corresponding PLNPs powder under 254 nm UV excitation. (c) Schematic illustrations of sensitive and specific persistent luminescent biotinylated PLNPs for the detection of avidin in the heterogeneous assay. Reproduced with permission from Ref. [64], © Royal Society of Chemistry 2017. (d) Schematic illustrations of the contributions of the interior and surface Cr^{3+} ions of the $ZnGaGeO_4:Cr^{3+}$ ratiometric luminescent nanothermometers to temperature sensing and *in vivo* bioimaging. Reproduced with permission from Ref. [71], © American Chemical Society 2017.

Apart from the above-mentioned Cr^{3+}-doped NIR PLNPs, Qiu's group also rationally designed and successfully fabricated $Zn_3Ga_2Sn_1O_8$:0.5 Cr^{3+} with remarkable long NIR PersL features by partially substituting Zn and Sn for Ga. The $Zn_3Ga_2Sn_1O_8$:0.5 Cr^{3+} phosphor shows bright NIR PersL and long decay time over 300 h, permitting a long-term, rechargeable and reliable deep tissue imaging. Moreover, the trap types of single ionized Zn interstitial and the Zn vacancy capturing an electron, and the larger deep trap concentrations also successfully verify the rationality of the material design [75]. Compared to Cr^{3+}-doped zinc gallogermanate NIR PLNPs, Cr^{3+}-doped non-gallate NIR PLNPs ($Zn_2SnO_4:Cr^{3+}$ and $Zn_{(2-x)}Al_{2x}Sn_{(1-x)}O_4:Cr^{3+}$) were also obtained, whose optical

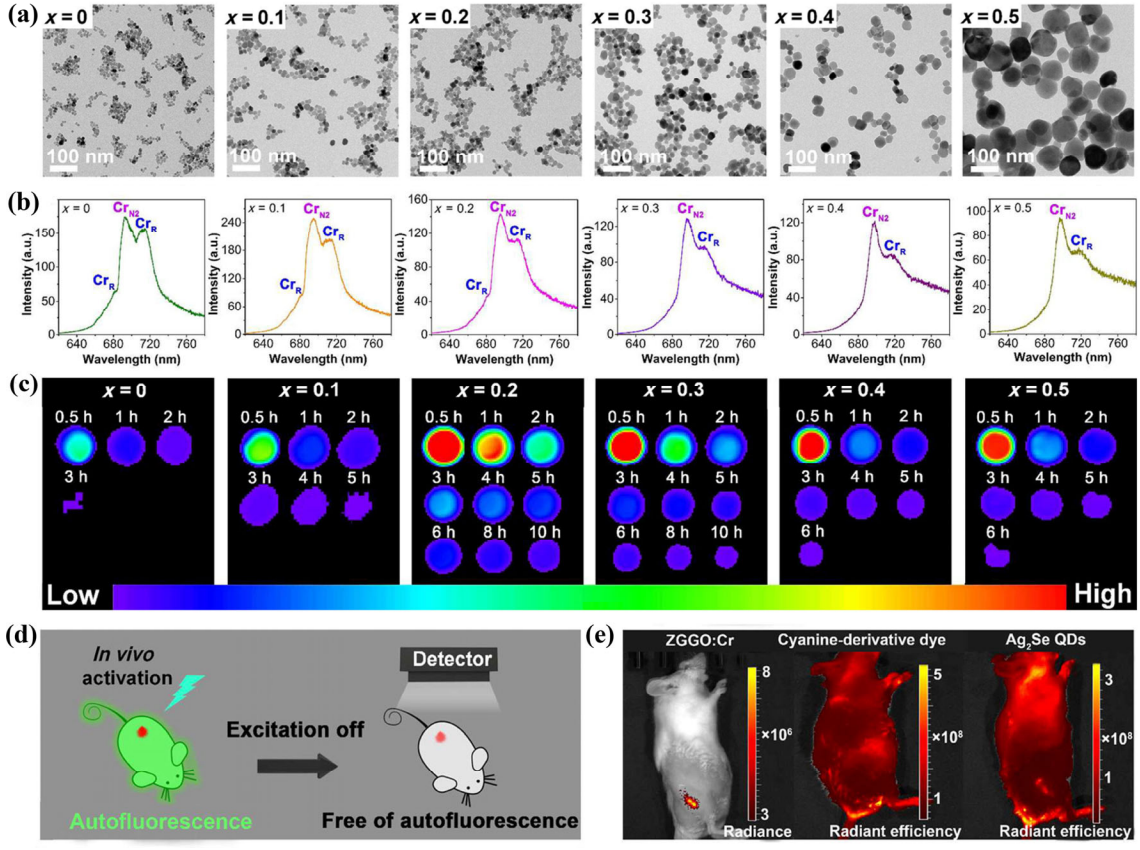

Figure 3 (a) TEM images, (b) photoluminescence spectrum and (c) PersL decay images of the $Zn_{1+x}Ga_{2-2x}Ge_xO_4$:Cr ($0 \le x \le 0.5$) nanoparticles. (d) Elimination of autofluorescence interference with ZGGO:Cr nanoparticles. (e) *In vivo* mice imaging with ZGGO:Cr ($x = 0.2$) nanoparticles, cyanine derivative dye, and Ag_2Se QDs. Reproduced with permission from Ref. [74], © American Chemical Society 2017.

characteristics of broad emission band range from 650 to 1,200 nm with the peaking at 800 nm and long luminescence time about 35 h [76]. This is because that Cr^{3+} can easy occupy the sites of Zn^{2+} and Sn^{4+} by non-equivalently substitution, Al dopant can precisely tailor the local crystal field of host materials and adjust the trap distribution in this system. Above all, Cr^{3+}-doped NIR PLNPs will open up new avenues for the exploration of more promising NIR PLNPs for medical imaging with superior resolution and low autofluorescence interference.

2.2 Mn^{2+}-doped NIR PLNPs

Mn^{2+} possesses an incompletely filled d shell and has a typical $3d^5$ electron configuration. Due to the involvement of the outermost d shells, the energy transitions of Mn^{2+} are considerably sensitive to the crystal/ligand field [77]. The interaction between Mn^{2+} ion surrounded by anions in different possible geometries (i.e., spherical, linear, square planar, tetrahedral, or octahedral) can be illustrated utilizing the crystal field theory. Mn^{2+} local environments in various crystallographic sites lead to the different distributions of the emission energies and generate a broad emission band varying from blue-green (490 nm) to NIR (750 nm) corresponding to the parity-forbidden 3d–3d intra-atomic transition from the lowest excited level $^4T_1$ (4G) to the ground state $^6A_1$ (6S). Green emission is produced by tetrahedral coordinated Mn^{2+} ion [78], whereas orange to red emission is given by octahedral coordinated Mn^{2+} ions [79, 80]. Thus, the emission strongly depends on the coordination number of Mn^{2+} in hosts.

In 2007, Daniel Scherman's group firstly reported Mn^{2+}-doped NIR PLNPs with maximum intensity ~ 690 nm. Compared with the red-emitting $MgSiO_3$:Eu^{2+},Dy^{3+},Mn^{2+}, the authors prepared $Ca_{0.2}Zn_{0.9}Mg_{0.9}Si_2O_6$:$Eu^{2+}$,$Dy^{3+}$,$Mn^{2+}$ phosphor and altered the composition of the host lattice by introducing Ca and Zn. In the phosphor, Dy^{3+} dopant acts as trap centres and Eu^{2+} as the primary acceptor of energy, respectively. The energy is subsequently released to Mn^{2+} ions through quantum tunneling and transfer processes under thermal stimulus. The symmetry and crystal field strength around the Mn^{2+} site change along with the composition changes in the host, thus generating the emission from red to NIR, corresponding to the well-known transition from $^4T_1$(4G) excited state to the $^6A_1$(6S) fundamental state [47]. To improve the persistent emission intensity/persistent time for *in vivo* long-term monitoring and diagnosis applications, the same group [81] synthesized several Mn^{2+}-doped diopside nanoparticles, either co-doped with trivalent lanthanide ions, e.g. $CaMgSi_2O_6$:Mn^{2+},Ln^{3+} (Ln^{3+}= Dy, Pr, Ce, Nd) (CMSO:Ln), or tridoped with Eu^{2+} and trivalent lanthanide ions, e.g. $CaMgSi_2O_6$:Mn^{2+},Eu^{2+},Ln^{3+} (CMSO:Eu,Ln) (Fig. 4). During irradiation, holes are mainly trapped by Mn^{2+} ions in Mg^{2+} sites, while electrons are trapped by oxygen vacancies and Ln^{3+} ions. Mn^{2+} emission from $^4T_1$ to $^6A_1$ occurs by thermally activated electrons release and capture by Mn^{3+}. Based on the different trap depths of Ln^{3+} ions on the NIR PersL properties of Mn^{2+}-doped CMSO, the authors verified that Pr3+ ions in tridoped CMSO diopside provide the optimal electron trap levels (~ 0.7 eV) below the conduction band edge and the recombination at room temperature responsible for the highest NIR PersL. Additional doping with Eu^{2+} not only allowed for sensitization to UV irradiation, critical for a suitable *in vivo* application, but also left the relative efficiency of electron traps unchanged. In conclusion, Daniel Scherman and coworks' pioneering works have greatly promoted the design of Mn^{2+}-doped NIR PLNPs and its application in biomedical field.

Apart from Mn^{2+}-doped silicate, Mn^{2+}-doped germanate as persistent luminescence materials are considerably studied. Usually, the PersL of Mn^{2+}-doped germanate mainly centered on visible light region. For example, Zn_2GeO_4:Mn^{2+} showed a green PersL [82, 83],

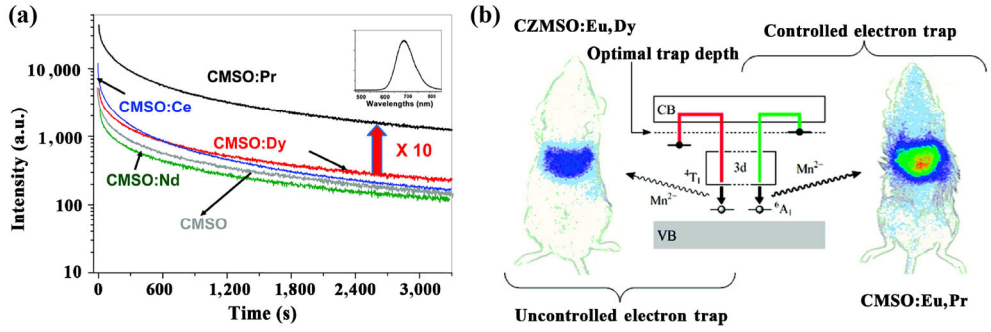

Figure 4 (a) Time-dependent Mn^{2+} luminescence intensity at 685 nm of CMSO and rare-earth co-doped CMSO:Ln compounds without further excitation after X-ray irradiation for 10 min. The inset shows the long-lasting phosphorescence spectrum. (b) Schematic energy level diagram of Mn^{2+} and Ln^{3+} in CZMSO and CMSO diopside PLNPs and *in vivo* imaging of different CZMSO and CMSO diopside PLNPs. Reproduced with permission from Ref. [81], © American Chemical Society 2011.

and $MgGeO_3$:Mn^{2+}; Li_2ZnGeO_4:Mn^{2+}, $CaZnGe_2O_6$:Mn^{2+} [84], etc. presented an orange-red PLNPs. To date, NIR PersL of Mn^{2+}-doped germanate was rarely reported. Inspiringly, Mn^{2+}-doped sodium gallium germanate ($Na(Al,Ga)Ge_3O_8$:Mn^2) glasses have been realized NIR PersL. The phosphors exhibit PersL in the spectral range from 600 to 800 nm, whose PersL can persist longer than 48 h at a dopant content of 0.1% Mn^{2+} (Fig. 5) [85]. When nanocrystalline high-albite $Na(Al,Ga)Ge_3O_8$ is precipitated from the supercooled melt through controlled thermal annealing, it can preserve the emission of Mn^{2+} ions, and in the meanwhile, the luminescence decay can be further improved more than 100 h. This originates from the introduction of Mn^{2+} at octahedral lattice sites with a more ionic bonding character in the nanocrystalline, and significantly increase defect density while decreasing depth. Owing to the prominent properties of Mn^{2+}-doped $Na(Al,Ga)Ge_3O_8$ nanocrystal, it may hold great promise for *in vivo* bioimaging or tumor therapy. Until now, only limited works have been developed and the design of Mn^{2+}-doped NIR PLNPs is still at the early stage. Currently, the reported Mn^{2+}-doped NIR PLNPs are also far from reaching the requirements in biomedical applications. Further development and expansion are still necessary in the follow-up research.

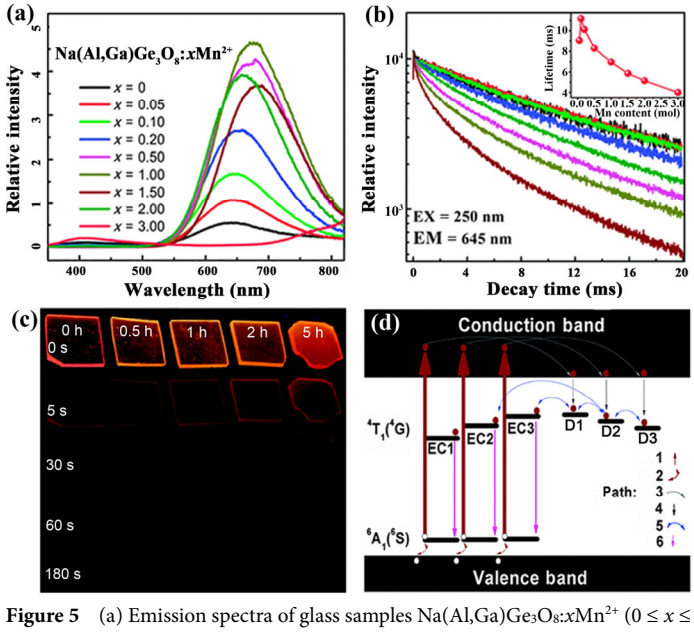

Figure 5 (a) Emission spectra of glass samples $Na(Al,Ga)Ge_3O_8$:xMn^{2+} ($0 \le x \le 0.5$) under excitation at 250 nm. (b) Emission decay curve for glass samples $Na(Al,Ga)Ge_3O_8$:xMn^{2+} ($0 \le x \le 0.5$). Inset: plot of lifetime to the Mn content x. (c) Photographs of glass samples $Na(Al,Ga)Ge_3O_8$:$0.1Mn^{2+}$ upon different crystallization time (0–5 h) and persistent time (0–180 s) after ceasing 254 nm excitation. (d) Schematic diagram of the possible mechanism leading to the red to ultralong NIR PersL from the Mn^{2+}-doped glasses and glass-ceramics. EC1, EC2 and EC3 represents the different types of octahedral Mn^{2+} emission centers; D1, D2 and D3 represents the different types of defects. Reproduced with permission from Ref. [85], © Royal Society of Chemistry 2015.

2.3 Mn^{4+}-doped NIR PLNPs

Mn^{4+} is another highly desirable NIR doping candidate because Mn^{4+} as same as Cr^{3+} ions possesses a $3d^3$ configuration in an octahedral coordination, showing a stabilized NIR emission from 600 to 800 nm [86, 87]. Once determining an activation ion, a proper host material capable of creating appropriate defects should be paid more attention to. Perovskite-type rare earth oxide is generally represented by the general formula of ABO_3, wherein the A site is occupied by the trivalent rare earth ions such as Y^{3+}, La^{3+} or Gd^{3+} ions, and the B site can be substituted by Al^{3+}, Ga^{3+} ion or Mg^{2+}/Zn^{2+}-Ti^{4+} pair. Luminescence performance will be improved and changed with the replacement of chemical units in the A, B site while the crystal structure remains essentially unchanged.

Due to the excellent ability of Mn^{4+} ions to substitute for Al^{3+}/Ga^{3+} ions in octahedral sites, aluminates/germanates are anticipated to be the greatest representative host for producing NIR PersL. Therein, inspired by the design of $CaTiO_3$:Pr^{3+} phosphor [88–90], Qiu et al. [91] developed a strategy and proposed a design concept for NIR PersL. The authors selected $MAlO_3$ (M = La, Gd) and Mn^{4+} as the host and emitter, respectively. They successfully fabricate a series of novel Mn^{4+}-doped $MAlO_3$ (M = La, Gd) phosphors with the emission maximum around 730 nm. By in-depth investigation of defect types and trap depths, the non-equivalent substitution of Mn^{4+} for Al^{3+} forms various defects including electron traps and hole traps. An improvement of long luminescence decay over 20 h is realized by co-doping Ge^{4+}/Mn^{4+}. The obtained imaging of deep pork tissues injected with $GdAlO_3$:$0.1\%Mn^{4+}$, $0.9\%Ge^{4+}$ phosphor reveals that the phosphors gives a very superior resolution at even 2 h post-injection and allow real-time bioimaging for tissue monitor more than 12 h (Figs. 6(a) and 6(b)).

Since the luminescence efficiency of $LaAlO_3$:Mn^{4+} is low, Poelman et al. proposed a charge compensation strategy with $Cl^-/Na^+/Ca^{2+}/Sr^{2+}/Ba^{2+}/Ge^{4+}$ co-dopants for enhancing the photoluminescence and PersL intensity performance [92]. Besides Mn^{4+}-doped $MAlO_3$ (M = La, Gd), Qiu's group further synthesized a novel non-rare-earth doped phosphor La_2MgGeO_6:Mn^{4+} with NIR PersL by solid-state reaction and proposed the possible luminescence mechanism to describe the long PersL behaviors in La_2MgGeO_6:Mn^{4+} phosphors (Figs. 6(c) and 6(d)). After UV light irradiation, electrons in the valence band are promoted to the conduction band, and simultaneously generate the hole traps. Mn^{4+} ions luminescence center obtains most of the excitation energy, producing a characteristic red emission, while the remaining part is subsequently captured by hole traps or electron traps. After stoppage of the irradiation, the trapped carriers are gradually released to the Mn^{4+} ions in the form of nonradiative transitions, resulting in the NIR PersL [93]. In addition, Hu group

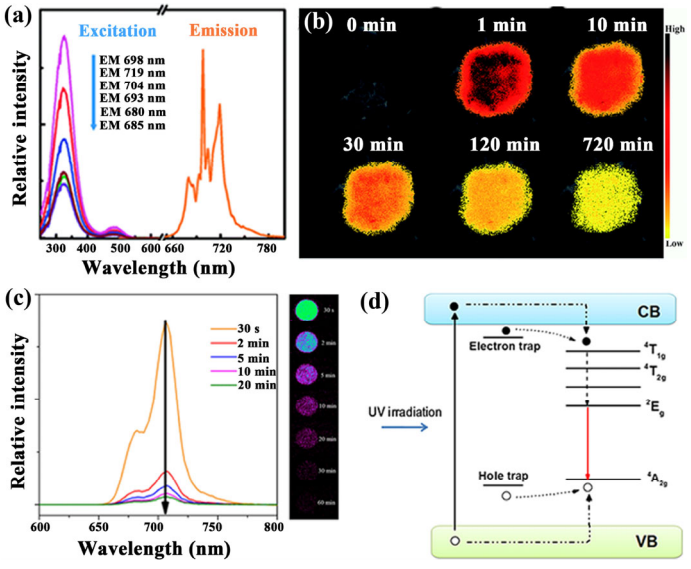

Figure 6 (a) Excitation and emission spectra spectra of $GdAlO_3$:0.1%Mn^{4+},0.9%Ge^{4+} sample. (b) Long PersL decay imaging of pork tissue. (Reproduced with permission from Ref. [91], © Royal Society of Chemistry 2014). (c) Long PersL spectra of La_2MgGeO_6:Mn^{4+} after removal of the UV lamp excitation for different decay time. Inset: the digital photographs of La_2MgGeO_6:Mn^{4+} samples pre-irradiated by UV lamp for 5 min for different decay time. (d) Schematic diagram of possible long PersL mechanism in La_2MgGeO_6:Mn^{4+}. Reproduced ith permission from Ref. [93], © The American Ceramic Society 2017.

also successfully synthesized non-rare-earth doped long-persistent phosphor: Mg_2GeO_4:Mn^{4+} with emission centered at 659 nm and lasting for 2 h [94]. The above-mentioned Mn^{4+}-doped NIR persistent materials will also broaden new horizons in fabricating novel NIR PLNPs and open the possibility of optical imaging with superior resolution and low autofluorescence interference.

3 Lanthanide ions-doped NIR PLNPs

Lanthanides have the same electronic configuration in both outer and sub-outer layer. Electrons are gradually filled into the 4f orbitals of lanthanides from $4f^0$ (for La) to $4f^{14}$ (for Lu). Benefited from their ladder-like dense energy level structures, lanthanides can generate emission ranging from the UV–visible to NIR regions [95, 96]. Since the effective shielding of 6s and 5p orbitals minimizes the ligand field effects, the luminescence of the lanthanides is mainly caused by electron redistribution within 4f orbitals. The electronic transitions within 4f orbitals are forbidden because of the violation of the Laporte rule, so the luminescent states of lanthanides are populated through energy transfer from a sensitizing host [97–101]. Thus, the emission of lanthanide ions-doped nanocrystals can be adjusted by varying both lanthanide emitters and host materials. Owing to the intersystem crossing and energy transfer processes between host and lanthanides, lanthanides display the extremely long-lived luminescence. However, the PersL of most lanthanide ions is usually located in visible region instead of NIR region. It is mainly due to the fact that the 5d state of the lanthanide is too high to be charged and it lacks carrier traps with a suitable defect types, depths, or distributions, etc. at room temperature. Before that, Bunzli et al. summarized some NIR PLNPs doped with lanthanide ions and their characteristic transitions in the NIR region [102, 103], where the main lanthanides such as Eu, Pr, Nd, Yb and Er mentioned can give prominent NIR PersL. Here we summarize the reported lanthanide ions-doped NIR PLNPs in recent years, including host, emitter, co-dopants, characteristic emission region and luminescence decay (Table 1).

Eu^{2+} ion is the most common luminescent center of lanthanide ions-doped phosphor. According to the crystal field effect (i.e. the main electrostatic effect of adjacent ions on Eu^{2+}), Eu^{2+} ions in solids have different emission wavelengths. A strong crystal field can reduce the lowest emission level of the $4f^6$ $5d^1$ electron configuration and produce yellow, orange, and red emission [23, 115]. Among them, the green $SrAl_2O_4$:Eu^{2+},Dy^{3+} and the blue $Sr_2MgSi_2O_7$: Eu^{2+},Dy^{3+} have been commercially available and are being widely used [116]. The research and development in Eu^{2+}-doped NIR PLNPs are far behind. On one hand, a concept of persistent energy transfer between two different emitting centers was proposed. In the energy transfer process, the emission spectrum overlaps between one and another emitting center in the same matrix, the later emitting center can be excited through persistent energy transfer to emit a longer wavelength persistence emission. Based on this, the most successful example for the Eu^{2+}-doped NIR PersL from emitting centers Eu^{2+} to Er^{3+} in the well-known $SrAl_2O_4$:Eu^{2+}, Dy^{3+} phosphor was realized [117]. On the other hand, suitable auxiliary dopants to create highly dense trapping levels is another well-developed strategy. For instance, Smet et al. [104] studied the PersL of Eu^{2+}-doped Ca_2SiS_4 co-doped with the rare-earth elements (Dy, Nd, Sm, or Tm). Only Ca_2SiS_4:Eu,Nd phosphor shows the strongest PersL at 660 nm, because the co-doping of Nd lead to the addition of infrared emission lines into the luminescence spectrum, originating from 4f–4f transitions within Nd^{3+}.

Table 1 Detail of host, emitter, co-dopants, emission region and luminescence decay of lanthanide ions-NIR PLNPs

Host	Emitter	Co-dopants	$\lambda_{emission}$ or emission region	Luminescence decay	References
Y_2O_3	Tm^{3+}	Yb^{3+}	~ 810 nm	—	[36]
	Ho^{3+}		~ 1,200 nm	—	
	Er^{3+}		1,000–1050 nm, ~1,530 nm		
$Y_3Al_2Ga_3O_{12}$	Er^{3+}	Ce^{3+},Cr^{3+}	1,450–1,670 nm	> 10 h	[49]
Ca_2SiS_4	Eu^{2+}	Nd^{3+}	660 nm	~ 18 min	[104]
$MgGeO_3$	Pr^{3+}		625, 900, 1,085 nm	> 120 h	[105]
$Ca_3Ga_2Ge_3O_{12}$	Pr^{3+}	Yb^{3+}	975 nm	> 100 h	[106]
$Sr_3Sn_2O_7$	Nd^{3+}		1,079 nm	1,000 s	[107]
$MgGeO_3$	Yb^{3+}		1,019 nm	> 100 h	[108]
$CaTiO_3$	Yb^{3+}	Bi^{3+}	~ 1,000 nm	> 80 h	[109]
$Ba_{0.8}AlSi_5O_2N_7$	Yb^{2+}		664 nm	300 s	[110]
$Gd_{2-x}RE_xO_2$ CO_3	Yb^{3+}		~ 1,000 nm	144 h	[111]
Ca_2SnO_4	Sm^{3+}		565, 610, 654 nm	30 min	[112]
$BaGd_2O_4$	Dy^{3+}		670, 763 nm	—	[113]
$Ca_4(PO_4)_2O$	Eu^{2+}	Y^{3+}	690 nm	> 200 s	[114]

Additionally, Yb displays parity-allowed 5d–4f transition and tunable emissions, enabling it to be another potential emitter for Yb-doped NIR PLNPs. Lanthanide ions-doped gadolinium oxycarbonates $Gd_{2-x}RE_xO_2CO_3$ (RE = Yb, Eu, Dy) were synthesized and the emission spectra were shown (Figs. 7(a)–7(c)) [111]. Among them, only Yb^{3+}-doped $Gd_2O_2CO_3$ has showed a significant NIR PersL at around 970 nm and exhibits a long luminescence decay time more than 6 days. The emission spectrum of Yb^{3+}-doped $Gd_2O_2CO_3$ at 970 nm is dominated by the $^2F_{7/2}$–$^2F_{5/2}$ transition of Yb^{3+} [118]. In contrast, the PersL intensity of both the Eu^{3+}- and Dy^{3+}-doped $Gd_2O_2CO_3$ is short-lived and extremely weak. The spectrum of Eu^{3+}-doped $Gd_2O_2CO_3$ shows a group of characteristic $^5D_0$–^7F_J transition of Eu^{3+} with the strongest emission peak of about 612 nm [119]. The emission lines of Dy^{3+}-doped $Gd_2O_2CO_3$ are ascribed to the $^4F_{9/2}$–^6H_J transitions of Dy^{3+} ion at around 575 nm [120]. Moreover, Xie et al. further reported that both Yb^{2+} and Yb^{3+} are considered as NIR PersL emitters to simultaneously exhibit strong PersL in the visible spectral region centered at 664 nm and NIR regions at 980 nm (Figs. 7(d)–7(f)) [110]. Trap centres in $Ba_{0.8}Sr_{0.2}AlSi_5O_2N_7$ phosphor are originated from the intrinsic defects of host material, which are caused by slight N/O ratio deviation during the synthesis process. The captured electrons are released to the lowest $4f^{13}5d^1$ excited state of Yb^{2+} ions via thermal assistance processes. Since the distance between the excited state of Yb^{2+} ($4f^{13}5d^1$) and the energy level of the host conduction band is very small, the $4f^{13}5d$–$4f^{14}$ transition of the Yb^{2+} ion causes the broad emission band centered at 664 nm. Meanwhile, the resonance energy transfer from Yb^{2+} to Yb^{3+} and the consequent $^2F_{5/2}$–$^2F_{7/2}$ transition of Yb^{3+}occurs leading to a typical sharp emission peak at 980 nm. Hence, Yb-doped NIR PLNPs can also be selected as another ideal optical probe for further deep-tissue bio-application to avoid the autofluorescence interference.

To date, the emission regions of NIR PLNPs are mostly located in the first bioimaging window (NIR-I, 650–950 nm). Dai and his group have recently shown NIR-II (~ 1,000–1,350 nm) fluorescence images recorded from deep-tissue anatomical imaging decorated with NIR-II probes have higher contrast compared to images recorded in the NIR-I window [121, 122]. Owing to the transitions from the excited state $^4F_{3/2}$ to different ^4I_J states (J = 9/2, 11/2, 13/2), Nd^{3+} ions have strong emission bands centered at 900, 1,060 and 1,340 nm and are well-suited for NIR-II optical imaging. OHNO et al. synthesized Nd^{3+}-doped $Sr_3Sn_2O_7$ of a double-layered perovskite structure with oxygen octahedral tilt and rotation, which emits an intense NIR-II luminescence from 4f–4f transition of Nd^{3+} [107]. Intriguingly, under the skin of chicken wings for biological imaging, the $Sr_3Sn_2O_7$:Nd^{3+} ceramic disk with a diameter of about 25 mm is invisible, while NIR PersL of the $Sr_3Sn_2O_7$:Nd^{3+} ceramic disk is clearly visible. Hence, the deep transmission of NIR-II wavelength enhances the image contrast of $Sr_3Sn_2O_7$:Nd^{3+}, which may have the potential to acquire the time-resolved imaging of internal structures with higher contrast.

Benefited from the typical $^4I_{13/2}$–$^4I_{15/2}$ transition at around 1,550 nm, Er^{3+} is also considered as the most promising emitter of NIR PLNPs whose emitting wavelength matches well with the NIR-III (~ 1,500–1,800 nm) window. As the above mentioned in Eu^{2+}-doped NIR PLNPs, the PersL from Er^{3+} through energy transfer from Eu^{2+} in the $SrAl_2O_4$:Eu^{2+},Dy^{3+} phosphor extend the emission wavelength [117]. However, after removing the UV excitation, the NIR PersL intensity and decay of the Er^{3+} emission at 1,530 nm is much weaker and shorter (less than 10 min) than the ultra-long PersL (more than 10 h) from Eu^{2+} in the green region. An successful example was promoted, where the $Y_3Al_2Ga_3O_{12}$:Er^{3+},Ce^{3+},Cr^{3+} exhibited long (more than 10 h) NIR-III PersL ranging from 1,450 to 1,670 nm through an efficient persistent energy transfer process form Ce^{3+} (Figs. 8(a)–8(c)) [49]. The excited electron of Ce^{3+} in the conduction band of $Y_3Al_2Ga_3O_{12}$ is trapped by the electron trapping center from Cr^{3+} and subsequently released from the formed Cr^{2+} trap with the thermal release back to the excited state of Ce^{3+}. The $5d_1$–$^2F_{5/2}$, $^2F_{7/2}$ transition of Ce^{3+} exhibit a broad band peaking at around 500 nm. At the same time, the resonance energy transfer process from Ce^{3+} to Er^{3+} takes place, which finally causes two intense sharp bands arising from the sharp NIR-I luminescence band (around 862) of

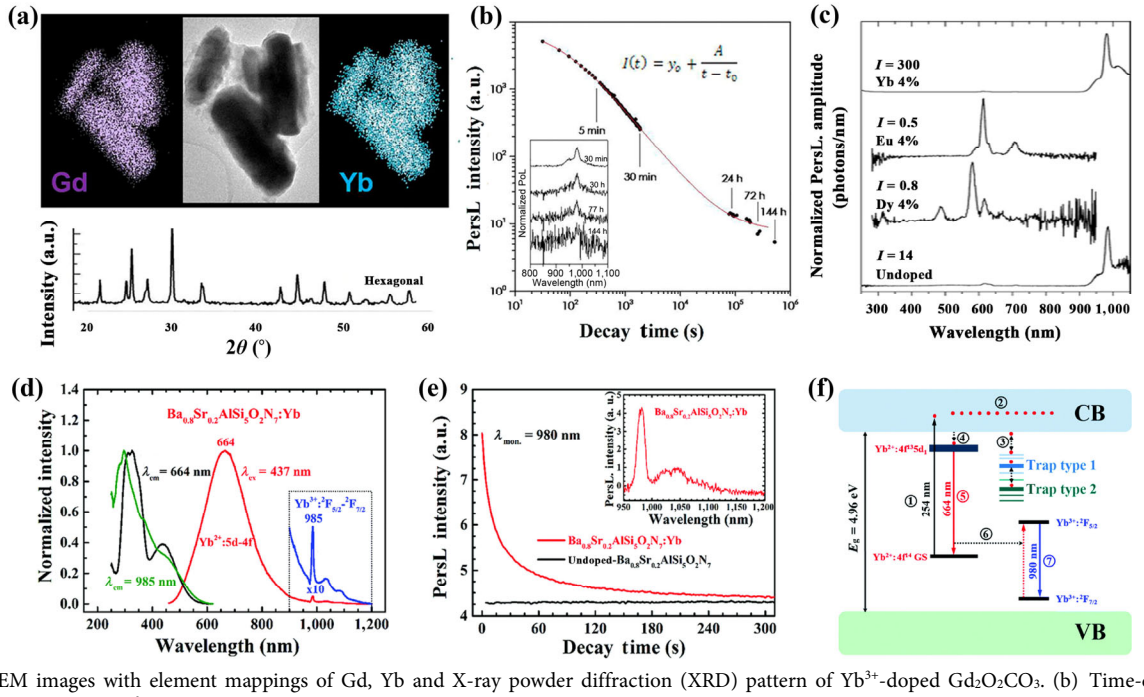

Figure 7 (a) TEM images with element mappings of Gd, Yb and X-ray powder diffraction (XRD) pattern of Yb^{3+}-doped $Gd_2O_2CO_3$. (b) Time-dependent long luminescence decay curve of Yb^{3+}-doped $Gd_2O_2CO_3$. The experimental data are fitted using a hyperbolic decay (red curve). (c) Normalized PersL emission spectra of different rare-earth elements doped $Gd_2O_2CO_3$ phosphors. Reproduced with permission from Ref. [111], © American Chemical Society 2014. (d) Normalized photoluminescence excitation and photoluminescence spectra of $Ba_{0.8}Sr_{0.2}AlSi_5O_2N_7$:Yb. (e) Long luminescence decay curves of Yb doped and undoped $Ba_{0.8}Sr_{0.2}AlSi_5O_2N_7$ ($\lambda_{mon.}$ = 980 nm). Inset: the PersL emission spectrum of $Ba_{0.8}Sr_{0.2}AlSi_5O_2N_7$:Yb from 950 to 1,200 nm after the removal of 254 nm excitation. (f) Schematic representation of the PersL mechanism of $Ba_{0.8}Sr_{0.2}AlSi_5O_2N_7$:Yb. Reproduced with permission from Ref. [110], © Royal Society of Chemistry 2017.

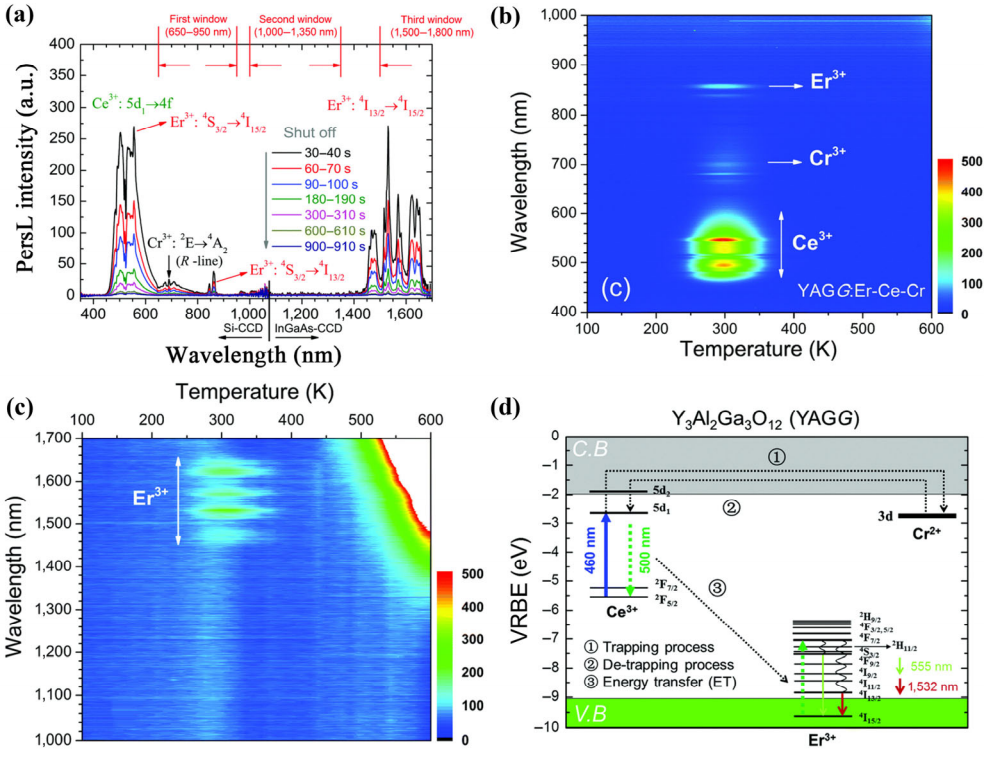

Figure 8 (a) PersL emission spectra of the $Y_3Al_2Ga_3O_{12}$:Er_{3+},Ce^{3+},Cr^{3+}. (b) and (c) Wavelength–temperature contour plots of the $Y_3Al_2Ga_3O_{12}$:Er^{3+},Ce^{3+},Cr^{3+} samples. (d) Schematic representation of the PersL mechanism for $Y_3Al_2Ga_3O_{12}$:Er^{3+},Ce^{3+},Cr^{3+} samples. Reproduced with permission from Ref. [49], © Royal Society of Chemistry 2016.

$^4S_{3/2}$–$^4I_{13/2}$ transitions of Er^{3+} and the broad NIR-III luminescence (around 1,532 nm) because of the typical $^4I_{13/2}$–$^4I_{15/2}$ transition of Er^{3+} (Fig. 8(d)). On account of improved optical resolution quality and deep tissue penetration depth in the NIR-III window, Er^{3+}-doped NIR PLNPs can be expected as a functionalized bioprobe for *in vivo* biosensing/bioimaging in the near future.

Among the known PLNPs, emitting centre ions play an important role in NIR PersL. Diversifying the emitting ions may be useful to advance the general comprehension of the phenomenon. At the same time, if the trap depth of holes or electrons can be controlled, we can reasonably design the capture and release process of charge carriers. It is theoretically significant for regulating the PersL properties in principle. In 2003, the energy level scheme for lanthanides in host, such as YPO_4, was firstly proposed by Dorenbos et al. [123]. The author presented that charge carriers trapped by trivalent lanthanide impurity are determined by the location of the ground state of the divalent and trivalent lanthanides relative to the valence and conduction bands of the host material. Afterwards, successful examples were demonstrated by Bos [124] and Bessiere et al. [24]. Ce^{3+}, Ln^{3+} co-doped or Pr^{3+}, Ln^{3+} co-doped YPO_4 can act as charge storage phosphors by a comprehensive thermally stimulated luminescence (TSL) study. The ground state energy of Ce^{3+} is above the valence band of YPO_4, which can trap a hole from the valence band from 25 to 700 °C. Ln^{3+} as electron traps released electrons into the conduction band. Recombination with charge carriers result in the characteristic 5d-4f emission of Ce^{3+} in the UV region. Pr^{3+} as another recombination center (and hole trap) plays a similar role to Ce^{3+} giving rise to red luminescence, which is highly consistent with the predicted position of its ground state relative to the valence band from the predicted energy level scheme. In addition, Lyu et al. deliberately designed storage phosphors through precisely controlling the release of electrons and holes based on the constructed vacuum referred binding energy (VRBE) diagrams and band gap engineering [125]. Figure 9(a) shows the constructed VRBE diagram of YPO_4 in the $4f^n$ ground state of trivalent and divalent lanthanides. The curves I and II link the VRBE of the ground state electrons of divalent and trivalent lanthanides, respectively. Such a diagram plays an important role in determining which shallow and deep electron–hole trap combinations to achieve the specific persistent phenomenon. The lanthanide related hole trap depth can

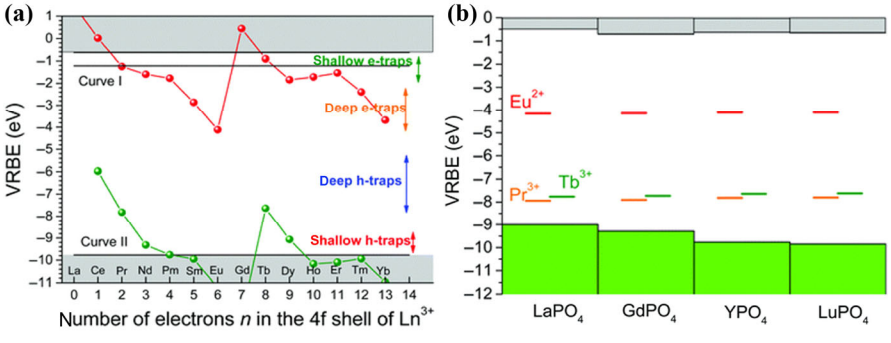

Figure 9 (a) VRBE diagram of the lanthanides with various traps depth in YPO_4. (b) Stacked VRBE diagram of $RePO_4$ with the binding energy in the ground states of Eu^{2+}, Pr^{3+}, and Tb^{3+}. Reproduced with permission from Ref. [125], © Royal Society of Chemistry 2018.

be tuned through tailoring the VRBE at the top of the valence band and electron trap depth can be engineered by altering the VRBE at the bottom of the conduction band (Fig. 9(b)) [126]. In a word, by gaining insight into the trap level position, the transport and capture of charge carriers, the regulation of conduction band and valence band provides a promising approach to design electron and hole traps for new optical storage and long NIR PersL phosphors.

4 Organic molecule-based NIR PLNPs

Most PLNPs are typically limited to metal-containing inorganic materials. The obtained inorganic PLNPs usually have some limitations. For example, the fabrication of inorganic PLNPs requires high temperatures over 1,000 °C and light scattering of inorganic host prevents the transparency of materials [50, 127]. The emission is controlled by slow release of trapped charge carriers from isolated traps of impurities, defects or ions through thermal stimulation, leading to low luminescence efficiency. In contrast, organic long-persistent luminescent (OLPL) systems, which are free from rare elements, have some more advantages than inorganic PLNPs in terms of solubility, transparency, flexibility and color tunability. The emission of OLPL originates from the recombination of long-lived charge-separated states of an exciplex, which forms between donor radical cations and acceptor radical anions. Under photo-excitation, donor molecule and acceptor molecule firstly form the charge-transfer states. Then, the generated radical ions of charge-transfer states diffuse by the hopping of charges and form the stable charge-separated states. After the stoppage of excitation, the separated charge carrier of the exciplex gradually recombine to generate long emission.

Recently, Adachi and coworkers developed OLPL materials by a simple mixture of electron-donor and electron-acceptor molecules, N,N,N,N'-tetramethylbenzidine (TMB) and 2,8-bis(diphenylphosphoryl) dibenzo[b,d]thiophene (PPT). The obtained OLPL materials exhibit long-lived luminescence for more than 1 h at room temperature, which endows them with the ability for *in vivo* bioimaging [1]. Owing to the low photoluminescence quantum yield of the above OLPL materials, slightly adding a little emitter dopants into the exciplex forming matrix was early studied to improve the quantum yield [128, 129]. Adachi's group tunes and enhances the OLPL emission of the same charge-separation matrix by doping different emitters, including 2,5,8,11-tetra-tert-butylperylene (TBPe), 9,10-bis[N,N-di-(ptolyl)-amino]anthracene (TTPA), 2,8-di-tert-butyl-5,11-bis(4-tertbutylphenyl)-6,12-diphenyltetracene (TBRb), tetraphenyldibenzoperiflanthene (DBP), and 4-(dicyanomethylene)-2-methyl-6-julolidyl-9-enyl-4H-pyran (DCM2) (Fig. 10(a)) [130]. The TMB and PPT molecules can immediately form charge-transfer states under photo-excitation and turns into a charge-separated state consisting of TMB radical cations and PPT radical anions. The charge-separated states can maintain for a long time at room temperature. Afterwards, the radical cation and the radical anion gradually recombine and form exciplexs in singlet and triplet states, which exhibit a broad emission ranging from greenish-blue to NIR. Such broad emission spectrum of the exciplex is sufficiently overlapped with the absorption spectrum of the emitter dopant, the energy of the generated exciplex can be transferred into the emitter dopant via FRET, which broadly tune long persistent luminescent emission (Figs. 10(b) and 10(c)). Based on this principle, the TMB:PPT:DCM2-based OLPL system show unprecedented advantages in achieving an extremely effective NIR PLNPs with superior resolution for autofluorescence-free bioimaging compared with TMB:PPT and TMB:PPT:TBPe (Figs. 10(d)–10(f)).

5 Semiconducting polymer self-assembled NIR PLNPs

Semiconductor polymer nanoparticles (SPNs) are a novel class of photonic nanomaterials, whose main component is semiconducting polymer with a π-electron delocalized backbones [131–133]. SPNs can produce very bright fluorescence, and the optical properties

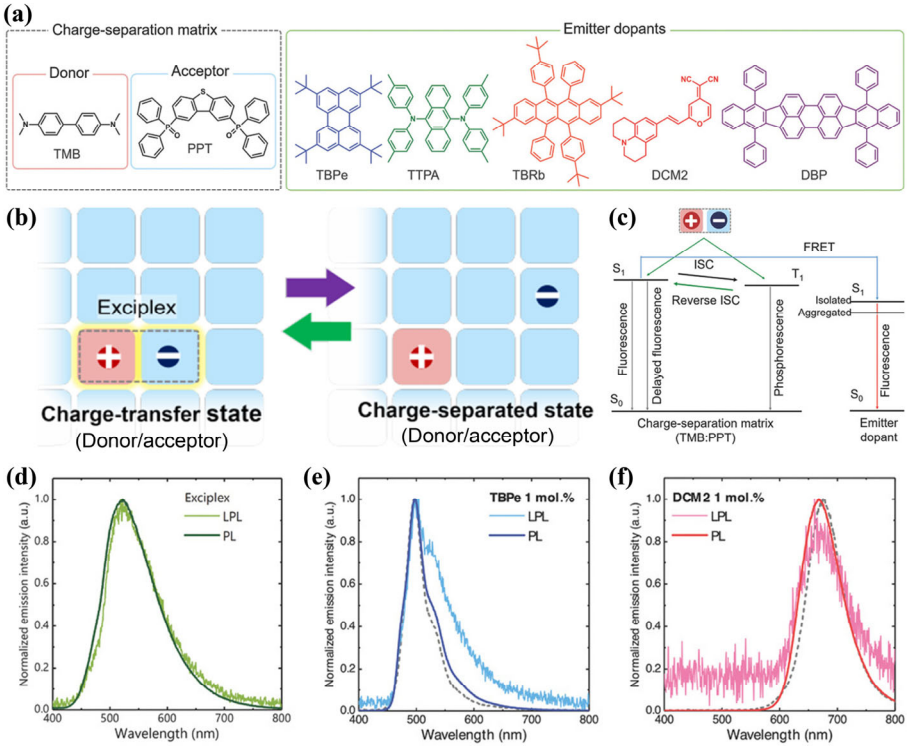

Figure 10 (a) Chemical structures of the electron donor (TMB), electron acceptor (PPT), and five different emitter dopants. (b) Emission mechanism of OLPL involved the form of charge-transfer state and the recombination a charge-separated state between TMB and PPT. (c) Energy level scheme of the charge-separation matrix and an emitter dopant. Steady-state photoluminescence and LPL emission spectra of (d) TMB:PPT, (e) TMB:PPT:TBPe, (f) TMB:PPT:DCM2. Reproduced with permission from Ref. [130], © WILEY-VCH Verlag GmbH & Co. KGaA, Weinheim 2018.

are primarily determined by the molecular structure of polymer nanoparticles. Since the band gap can be turned by monomers used for polymerization, SPN is also widely used as a highly sensitive chemical and bioluminescent probe to meet different imaging requirements [134–136]. Rao et al. firstly used nano-precipitation of MEHPPV, PS-PEG-COOH and NIR775 to synthesize the biocompatible SPNs, which can emit NIR PersL with nearly 1 h decay time after the stoppage of white light excitation (Fig. 11(a)) [137]. Compared to the undoped nanoparticles, the MEHPPV emission at 500–700 nm significantly decrease in the NIR775-doped nanoparticles, indicating effective energy transfer from the MEHPPV polymer to the NIR775 dye via FRET. In the NIR775-doped polymer nanoparticle, both fluorescence spectrum and PersL spectrum show a broad emission at 500–700 nm and a sharp peak at 780 nm (Fig. 11(b)). The semiconductor layer of the polymer can be effectively activated by white light excitation and then captures the excitation energy. The energy gradually release from the trap and was transferred to the NIR775, generating NIR PersL. Due to extremely low background interference, the NIR PersL imaging offers much improved signal-to-noise ratio compared with fluorescence imaging by injecting NIR775-doped MEHPPV polymer nanoparticles into the mice (Fig. 11(c)). This creative work indicates the potential of semiconducting polymer self-assembled NIR PLNPs for auto-fluorescence-free *in vivo* imaging.

Although Rao et al. observed the NIR PersL phenomenon in SPNs, it has not been explored whether the long PersL signal of SPNs from chemical structure or nanoparticle structure. Pu et al [138] designed SPNs with different molecular structures and further investigated the PersL mechanism. The authors found that only some phenylenevinylene (PPV)-based SPNs with electron-donating substituents show obvious PersL, which involves $^1O_2$-induced formation of unstable chemical defects from a PPV-dioxetane intermediate. Such unstable intermediate can spontaneously degrade into a PPV-aldehyde to generate photons, confirming that the chemical structure rather than the nanoparticle structure determines the NIR PersL of SPNs. To effectively amplify and redshift the NIR PersL of SPNs, silicon 2,3-naphthalocyanine bis(trihexylsilyloxide) (NCBS) as $^1O_2$ producer and NIR emitter was doped into MEHPPV (Fig. 12(a)).

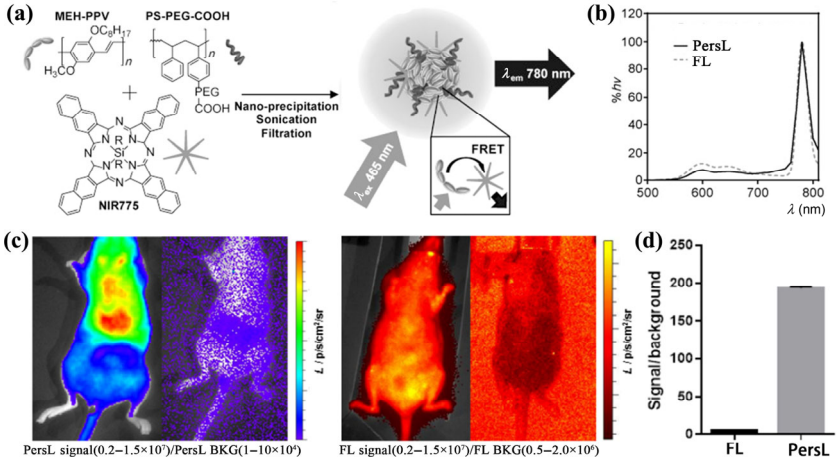

Figure 11 (a) Schematic of nano-precipitation of MEH-PPV nanoparticles doped with NIR775 and fluorescence (FL) and PersL spectra of MEH-PPV nanoparticles doped with NIR775 because of the Förster resonance energy transfer (FRET). (b) Comparison of signal-to-noise ratio of *in vivo* PersL and FL imaging after intravenous injection of the nanoparticles. Reproduced with permission from Ref. [137], © Wiley-VCH VerlagGmbH &Co. KGaA,Weinheim 2015.

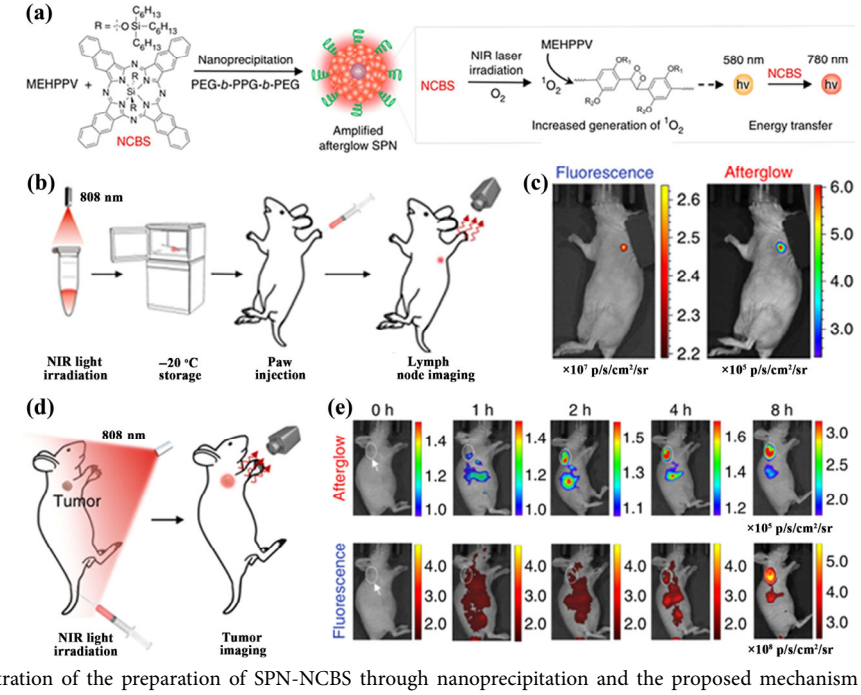

Figure 12 (a) Schematic illustration of the preparation of SPN-NCBS through nanoprecipitation and the proposed mechanism for $^1O_2$-sensitizer-amplified NIR PersL. (b) Schematic illustration of lymph node PersL imaging. (c) *In vivo* fluorescence and PersL imaging of a lymph node after intradermal injection of SPN-NCBS5 into the forepaw of mouse. (d) Schematic illustration of PersL imaging of HeLa tumor-bearing mice. (e) *In vivo* PersL and fluorescence images of HeLa tumor-bearing mice after intravenous injection of SPN-NCBS5. Reproduced with permission from Ref. [138], © Nature Publishing Group 2017.

Due to the efficient energy transfer from MEHPPV to NCBS, the MEHPPV fluorescence at 580 nm gradually decreased, while NIR PersL of NCBS at 775 nm gradually increase with increasing doping concentration. When NCBS-doped MEHPPV was used to real-time mapping of lymph nodes, the signal-to-noise ratio of PersL image substantially increased to 127-fold than fluorescence image (Figs. 12(b) and 12(c)). After injected into tail vein of HeLa tumor-bearing mice, both NIR PersL and NIR fluorescence signals in the tumor site gradually increased over time. Also, the signal-to-noise ratio of NIR PersL images was higher than that of NIR fluorescence images in all time points, 23.3 times higher than that of NIR fluorescence image at t = 2 h (Figs. 12(d) and 12(e)). In addition to the above mentioned MEHPPV-based SPNs, the same group further promoted the application for ultrasensitive imaging of metastatic tumors in living mice with amphiphilic poly(p-phenylenevinylene) derivatives that self-assemble into the nanoagent (SPPVN) [139]. Therefore, with superior contrast in imaging of NIR dye-doped SPNs, more and more semiconducting polymer self-assembled NIR PLNPs and advanced scientific applications should be explored.

6 Conclusion and outlook

Over the past decades, PLNPs have attracted a wide range of attention in autofluorescence-free biosensing/bioimaging. In this review, we mainly focused on the different types of NIR PLNPs for biomedical applications. The design, fabrication and biological application of transition metal ions-doped NIR PLNPs, lanthanide ions-doped NIR PLNPs, organic molecules-based NIR PLNPs, and semiconducting polymer self-assembled NIR PLNPs and their biological application were summarized. Owing to the reduced scattering and absorption coefficient in penetrating biological organs or tissues, NIR PLNPs possess deep tissue penetration. Therefore, NIR PLNPs are ideal for *in vivo* biosensing/bioimaging with superior resolution and sensitivity. Although different kinds of NIR PLNPs are extensively studied to achieve better biological application, lots of efforts are still desired in many areas, such as (1) development of NIR PLNPs that can be charged by visible or even NIR light. NIR PLNPs in long-term biosensing/bioimaging is limited by UV irradiation with low penetration depth and high cellular damage. (2) Expansion of the emission band of NIR PLNPs to the second or third transparent window. The longer NIR PersL can improve the detection sensitivity of biomarkers for different diseases. (3) Improvement of PersL intensity and persistent decay time. Usually, emitting centres with lower fluorescence quantum efficiency will result in the decrease of PersL intensity, but defect properties (defect types, depths, or distributions etc.) and conduction band engineering, can significantly tune the luminescence properties. For example, the PersL intensity of Eu^{3+} co-doped $MgGeO_3$:Mn^{2+} increased with increasing Zn content, while that of Yb^{3+} co-doped phosphors decreased, resulting from lowering the bottom of the conduction band relative to the ground state of the divalent lanthanide ions [140]. (4) Exploration of the new activators and matrices. The center and corresponding host of NIR PLNPs are very limited, especially OLPL systems. For Cr^{3+}-doped NIR PLNPs, only gallates can be used as the suitable hosts to effectively generate NIR PersL. In addition to the gallates, aluminates and silicates, it is expected to discover new persistent luminescent matrices. For NIR OLPL systems, only TMB:PPT was reported as charge-separation matrix. In a word, to take full advantage of PLNPs for *in vivo* biosensing/bioimaging, the considerable strategies are altering the crystal structure of the host material to regulate the trap types and trap depth, selecting proper emitters for effective radiative transition as well as transferring energy of sensitizers to acceptors to tune long NIR PersL, which have been proposed as the important and considerable factors for rationally engineering NIR PLNPs.

Acknowledgements

This work was supported by the National Natural Science Foundation of China (NSFC, No. 21675120), the National Key R&D Program of China (Nos. 2017YFA0208000 and 2016YFF0100800), Foundation for Innovative Research Groups of NSFC (No. 21521063), and the National Basic Research Program of China (No. 2015CB932600).

References

[1] Kabe, R.; Adachi, C. Organic long persistent luminescence. *Nature* **2017**, *550*, 384–387.

[2] Zagorovsky, K.; Chan, W. C. W. Illuminating the deep. *Nat. Mater.* **2013**, *12*, 285–287.

[3] Vahrmeijer, A. L.; Hutteman, M.; van der Vorst, J. R.; van de Velde, C. J. H.; Frangioni, J. V. Image-guided cancer surgery using near-infrared fluorescence. *Nat. Rev. Clin. Oncol.* **2013**, *10*, 507–518.

[4] Zwier, J. M.; Hildebrandt, N. Time-gated FRET detection for multiplexed biosensing. In *Reviews in Fluorescence 2016*. Geddes, C. D., Ed.; Springer: Cham, 2017; pp 17–43.

[5] Baggaley, E.; Weinstein, J. A.; Williams, J. A. G. Time-resolved emission imaging microscopy using phosphorescent metal complexes: Taking FLIM and PLIM to new lengths. In *Luminescent and Photoactive Transition Metal Complexes as Biomolecular Probes and Cellular Reagents*. Lo, K. K. W., Ed.; Springer: Berlin Heidelberg, 2014; p 1.

[6] Maldiney, T.; Bessière, A.; Seguin, J.; Teston, E.; Sharma, S. K.; Viana, B.; Bos, A. J. J.; Dorenbos, P.; Bessodes, M.; Gourier, D. et al. The *in vivo* activation of persistent nanophosphors for optical imaging of vascularization, tumours and grafted cells. *Nat. Mater.* **2014**, *13*, 418–426.

[7] Berezin, M. Y.; Achilefu, S. Fluorescence lifetime measurements and biological imaging. *Chem. Rev.* **2010**, *110*, 2641–2684.

[8] Chen, Y.; Periasamy, A. Characterization of two-photon excitation fluorescence lifetime imaging microscopy for protein localization. *Microsc. Res. Tech.* **2004**, *63*, 72–80.

[9] Zhang, K. Y.; Yu, Q.; Wei, H. J.; Liu, S. J.; Zhao, Q.; Huang, W. Long-lived emissive probes for time-resolved photoluminescence bioimaging and biosensing. *Chem. Rev.* **2018**, *118*, 1770–1839.

[10] van den Eeckhout, K.; Smet, P. F.; Poelman, D. Persistent luminescence in Eu^{2+}-doped compounds: A review. *Materials* **2010**, *3*, 2536–2566.

[11] Matsuzawa, T.; Aoki, Y.; Takeuchi, N.; Murayama, Y. A new long phosphorescent phosphor with high brightness, $SrAl_2O_4$: Eu^{2+}, Dy^{3+}. *J. Electrochem. Soc.* **1996**, *143*, 2670–2673.

[12] Sun, H. B.; Liu, S. J.; Lin, W. P.; Zhang, K. Y.; Lv, W.; Huang, X.; Huo, F. W.; Yang, H. R.; Jenkins, G.; Zhao, Q. et al. Smart responsive phosphorescent materials for data recording and security protection. *Nat. Commun.* **2014**, *5*, 3601.

[13] Hanaoka, K.; Kikuchi, K.; Kobayashi, S.; Nagano, T. Time-resolved long-lived luminescence imaging method employing luminescent lanthanide probes with a new microscopy system. *J. Am. Chem. Soc.* **2007**, *129*, 13502–13509.

[14] Baggaley, E.; Botchway, S. W.; Haycock, J. W.; Morris, H.; Sazanovich, I. V.; Williams, J. A. G.; Weinstein, J. A. Long-lived metal complexes open up microsecond lifetime imaging microscopy under multiphoton excitation: From FLIM to PLIM and beyond. *Chem. Sci.* **2014**, *5*, 879–886.

[15] Li, L.; Pandey, A.; Werder, D. J.; Khanal, B. P.; Pietryga, J. M.; Klimov, V. I. Efficient synthesis of highly luminescent copper indium sulfide-based core/shell nanocrystals with surprisingly long-lived emission. *J. Am. Chem. Soc.* **2011**, *133*, 1176–1179.

[16] Raut, S. L.; Fudala, R.; Rich, R.; Kokate, R. A.; Chib, R.; Gryczynski, Z.; Gryczynski, I. Long lived BSA Au clusters as a time gated intensity imaging probe. *Nanoscale* **2014**, *6*, 2594–2597.

[17] Kandpal, S. K.; Goundie, B.; Wright, J.; Pollock, R. A.; Mason, M. D.; Meulenberg, R. W. Investigation of the emission mechanism in milled $SrAl_2O_4$: Eu, Dy using optical and synchrotron X-ray spectroscopy. *ACS Appl. Mater. Interfaces* **2011**, *3*, 3482–3486.

[18] Wang, J.; Ma, Q. Q.; Liu, H. Y.; Wang, Y. Q.; Shen, H. J.; Hu, X. X; Ma, C.; Yuan, Q.; Tan, W. H. Time-gated imaging of latent fingerprints and specific visualization of protein secretions via molecular recognition. *Anal. Chem.* **2017**, *89*, 12764–12770.

[19] Li, Z. J.; Zhang, Y. W.; Wu, X.; Huang, L.; Li, D. S.; Fan, W.; Han, G. Direct aqueous-phase synthesis of sub-10 nm "luminous pearls" with enhanced *in vivo* renewable near-infrared persistent luminescence. *J. Am. Chem. Soc.*

2015, *137*, 5304–5307.
[20] Aitasalo, T.; Hietikko, A.; Hreniak, D.; Hölsä, J.; Lastusaari, M.; Niittykoski, J.; Stręk, W. Luminescence properties of $BaMg_2Si_2O_7$: Eu^{2+}, Mn^{2+}. *J. Alloys Compd*. **2008**, *451*, 229–231.
[21] Lin, X. H.; Zhang, R. L.; Tian, X. M.; Li, Y.; Du, B. S.; Nie, J. M.; Li, Z. Z.; Chen, L.; Ren, J. J.; Qiu, J. R. et al. Coordination geometry-dependent multi-band emission and atypically deep-trap-dominated NIR persistent luminescence from chromium-doped aluminates. *Adv. Opt. Mater*. **2018**, *6*, 1701161.
[22] Zhang, Y.; Huang, R.; Lin, Z. X.; Song, J.; Wang, X.; Guo, Y. Q.; Song, C.; Yu, Y. Co-dopant influence on near-infrared luminescence properties of Zn_2SnO_4: Cr^{3+}, Eu^{3+} ceramic discs. *J. Alloys Compd*. **2016**, *686*, 407–412.
[23] Jia, D. D.; Jia, W. Y.; Evans, D. R.; Dennis, W. M.; Liu, H. M.; Zhu, J.; Yen, W. M. Trapping processes in CaS: Eu^{2+}, Tm^{3+}. *J. Appl. Phys*. **2000**, *88*, 3402–3407.
[24] Lecointre, A.; Bessière, A.; Bos, A. J. J.; Dorenbos, P.; Viana, B.; Jacquart, S. Designing a red persistent luminescence phosphor: The example of YPO_4: Pr^{3+}, Ln^{3+} (Ln = Nd, Er, Ho, Dy). *J. Phys. Chem. C* **2011**, *115*, 4217–4227.
[25] Zheng, B.; Chen, H. B.; Zhao, P. Q.; Pan, H. Z.; Wu, X. L.; Gong, X. Q.; Wang, H. J.; Chang, J. Persistent luminescent nanocarrier as an accurate tracker *in vivo* for near infrared-remote selectively triggered photothermal therapy. *ACS Appl. Mater. Interfaces* **2016**, *8*, 21603–21611.
[26] Zhang, H. W.; Fu, X. Y.; Niu, S. Y.; Xin, Q. Blue luminescence of nanocrystalline $CaZrO_3$: Tm phosphors synthesized by a modified Pechini sol–gel method. *J. Lumin*. **2008**, *128*, 1348–1352.
[27] Wu, Y. L.; Li, Y.; Qin, X. X.; Chen, R. C.; Wu, D. K.; Liu, S. J.; Qiu, J. R. Dual mode NIR long persistent phosphorescence and NIR-to-NIR Stokes luminescence in $La_3Ga_5GeO_{14}$: Cr^{3+}, Nd^{3+} phosphor. *J. Alloys Compd*. **2015**, *649*, 62–66.
[28] Kong, J. T.; Zheng, W.; Liu, Y. S.; Li, R. F.; Ma, E.; Zhu, H. M.; Chen, X. Y. Persistent luminescence from Eu^{3+} in SnO_2 nanoparticles. *Nanoscale* **2015**, *7*, 11048–11054.
[29] Abdukayum, A.; Chen, J. T.; Zhao, Q.; Yan, X. P. Functional near infrared-emitting Cr^{3+}/Pr^{3+} co-doped zinc gallogermanate persistent luminescent nanoparticles with superlong afterglow for *in vivo* targeted bioimaging. *J. Am. Chem. Soc*. **2013**, *135*, 14125–14133.
[30] Ma, Q. Q.; Wang, J.; Zheng, W.; Wang, Q.; Li, Z. H.; Cong, H. J.; Liu, H. J.; Chen, X. Y.; Yuan, Q. Controlling disorder in host lattice by hetero-valence ion doping to manipulate luminescence in spinel solid solution phosphors. *Sci. China Chem*. **2018**, *61*, 1624–1629.
[31] Liu, H. Y.; Hu, X. X.; Wang, J.; Liu, M.; Wei, W.; Yuan, Q. Direct low-temperature synthesis of ultralong persistent luminescence nanobelts based on a biphasic solution-chemical reaction. *Chin. Chem. Lett*. **2018**, *29*, 1641–1644.
[32] Song, L.; Li, P. P.; Yang, W.; Lin, X. H.; Liang, H.; Chen, X. F.; Liu, G.; Li, J.; Yang, H. H. Low-dose X-ray activation of W(VI)-doped persistent luminescence nanoparticles for deep-tissue photodynamic therapy. *Adv. Funct. Mater*. **2018**, *28*, 1707496.
[33] Wang, X. J.; Jia, D. D.; Yen, W. M. Mn^{2+} activated green, yellow, and red long persistent phosphors. *J. Lumin*. **2003**, *102–103*, 34–37.
[34] Zheng, B.; Bai, Y.; Chen, H. B.; Pan, H. Z.; Ji, W. Y.; Gong, X. Q.; Wu, X. L.; Wang, H. J.; Chang, J. Near-infrared light-excited upconverting persistent nanophosphors *in vivo* for imaging-guided cell therapy. *ACS Appl. Mater. Interfaces* **2018**, *10*, 19514–19522.
[35] Song, L.; Lin, X. H.; Song, X. R.; Chen, S.; Chen, X. F.; Li, J.; Yang, H. H. Repeatable deep-tissue activation of persistent luminescent nanoparticles by soft X-ray for high sensitivity long-term *in vivo* bioimaging. *Nanoscale* **2017**, *9*, 2718–2722.
[36] Niioka, H.; Yamasaki, J.; Dung, D. T. K.; Miyake, J. Enhancement of near-infrared luminescence of Y_2O_3: Ln, Yb (Ln = Tm, Ho, Er) by Li-ion doping for cellular bioimaging. *Chem. Lett*. **2016**, *45*, 1406–1408.
[37] Wang, B.; Lin, H.; Xu, J.; Chen, H.; Lin, Z. B.; Huang, F.; Wang, Y. S. Design, preparation, and characterization of a novel red long-persistent perovskite phosphor: $Ca_3Ti_2O_7$: Pr^{3+}. *Inorg. Chem*. **2015**, *54*, 11299–11306.
[38] Wang, Y. Q.; Wang, J.; Ma, Q. Q.; Li, Z. H.; Yuan, Q. Recent progress in background-free latent fingerprint imaging. *Nano Res*. **2018**, *11*, 5499–5518.
[39] Li, N.; Li, Y. H.; Han, Y. Y.; Pan, W.; Zhang, T. T.; Tang, B. A highly selective and instantaneous nanoprobe for detection and imaging of ascorbic acid in living cells and *in vivo*. *Anal. Chem*. **2014**, *86*, 3924–3930.
[40] Abdukayum, A.; Yang, C. X.; Zhao, Q.; Chen, J. T.; Dong, L. X.; Yan, X. P. Gadolinium complexes functionalized persistent luminescent nanoparticles as a multimodal probe for near-infrared luminescence and magnetic resonance imaging *in vivo*. *Anal. Chem*. **2014**, *86*, 4096–4101.
[41] Shi, J. P.; Sun, X.; Li, J. L.; Man, H. Z.; Shen, J. S.; Yu, Y. K.; Zhang, H. W. Multifunctional near infrared-emitting long-persistence luminescent nanoprobes for drug delivery and targeted tumor imaging. *Biomaterials* **2015**, *37*, 260–270.
[42] Teng, Y.; Zhou, J. J.; Khisro, S. N.; Zhou, S. F.; Qiu, J. R. Persistent luminescence of $SrAl_2O_4$: Eu^{2+}, Dy^{3+}, Cr^{3+} phosphors in the tissue transparency window. *Mater. Chem. Phys*. **2014**, *147*, 772–776.
[43] Wu, S. Q.; Chi, C. W.; Yang, C. X.; Yan, X. P. Penetrating peptide-bioconjugated persistent nanophosphors for long-term tracking of adipose-derived stem cells with superior signal-to-noise ratio. *Anal. Chem*. **2016**, *88*, 4114–4121.
[44] Lu, Y. C.; Yang, C. X.; Yan, X. P. Radiopaque tantalum oxide coated persistent luminescent nanoparticles as multimodal probes for *in vivo* near-infrared luminescence and computed tomography bioimaging. *Nanoscale* **2015**, *7*, 17929–17937.
[45] Fu, X. Y.; Liu, C. L.; Shi, J. P.; Man, H. Z.; Xu, J.; Zhang, H. W. Long persistent near infrared luminescence nanoprobes $LiGa_5O_8$: Cr^{3+}-PEG-OCH_3 for *in vivo* imaging. *Opt. Mater*. **2014**, *36*, 1792–1797.
[46] Nie, J. M.; Li, Y.; Liu, S. S.; Chen, Q. Q.; Xu, Q.; Qiu, J. R. Tunable long persistent luminescence in the second near-infrared window via crystal field control. *Sci. Rep*. **2017**, *7*, 12392.
[47] le Masne de Chermont, Q.; Chanéac, C.; Seguin, J.; Pellé, F.; Maîtrejean, S.; Jolivet, J. P.; Gourier, D.; Bessodes, M.; Scherman, D. Nanoprobes with near-infrared persistent luminescence for *in vivo* imaging. *Proc. Natl. Acad. Sci. USA* **2007**, *104*, 9266–9271.
[48] Lin, X. H.; Song, L.; Chen, S.; Chen, X. F.; Wei, J. J.; Li, J. Y.; Huang, G. M.; Yang, H. H. Kiwifruit-like persistent luminescent nanoparticles with high-performance and *in situ* activable near-infrared persistent luminescence for long-term *in vivo* bioimaging. *ACS Appl. Mater. Interfaces* **2017**, *9*, 41181–41187.
[49] Xu, J.; Murata, D.; Ueda, J.; Tanabe, S. Near-infrared long persistent luminescence of Er^{3+} in garnet for the third bio-imaging window. *J. Mater. Chem. C* **2016**, *4*, 11096–11103.
[50] Li, Y.; Gecevicius, M.; Qiu, J. R. Long persistent phosphors—From fundamentals to applications. *Chem. Soc. Rev*. **2016**, *45*, 2090–2136.
[51] Lécuyer, T.; Teston, E.; Ramirez-Garcia, G.; Maldiney, T.; Viana, B.; Seguin, J.; Mignet, N.; Scherman, D.; Richard, C. Chemically engineered persistent luminescence nanoprobes for bioimaging. *Theranostics* **2016**, *6*, 2488–2524.
[52] Sun, S. K.; Wang, H. F.; Yan, X. P. Engineering persistent luminescence nanoparticles for biological applications: From biosensing/bioimaging to theranostics. *Acc. Chem. Res*. **2018**, *51*, 1131–1143.
[53] Wang, J.; Ma, Q. Q.; Wang, Y. Q.; Shen, H. J.; Yuan, Q. Recent progress in biomedical applications of persistent luminescence nanoparticles. *Nanoscale* **2017**, *9*, 6204–6218.
[54] Singh, S. K. Red and near infrared persistent luminescence nano-probes for bioimaging and targeting applications. *RSC Adv*. **2014**, *4*, 58674–58698.
[55] Elzerman, J. M.; Hanson, R.; Willems van Beveren, L. H.; Witkamp, B.; Vandersypen, L. M. K.; Kouwenhoven, L. P. Single-shot read-out of an individual electron spin in a quantum dot. *Nature* **2004**, *430*, 431–435.
[56] Zubiaga, A.; Plazaola, F.; García, J. A.; Tuomisto, F.; Muñoz-Sanjosé, V.; Tena-Zaera, R. Positron annihilation lifetime spectroscopy of ZnO bulk samples. *Phys. Rev. B* **2007**, *76*, 085202.
[57] Dutta, S.; Chattopadhyay, S.; Sarkar, A.; Chakrabarti, M.; Sanyal, D.; Jana, D. Role of defects in tailoring structural, electrical and optical properties of ZnO. *Prog. Mater. Sci*. **2009**, *54*, 89–136.
[58] Bioul, G.; Davio, M. Taylor expansions of Boolean functions and of their derivatives. *Philips Res. Rep*. **1972**, *27*, 1–6.
[59] Bessière, A.; Jacquart, S.; Priolkar, K.; Lecointre, A.; Viana, B.; Gourier, D. $ZnGa_2O_4$: Cr^{3+}: A new red long-lasting phosphor with high brightness. *Opt. Express* **2011**, *19*, 10131–10137.
[60] Allix, M.; Chenu, S.; Véron, E.; Poumeyrol, T.; Kouadri-Boudjelthia, E. A.; Alahraché, S.; Porcher, F.; Massiot, D.; Fayon, F. Considerable improvement of long-persistent luminescence in germanium and tin substituted $ZnGa_2O_4$. *Chem. Mater*. **2013**, *25*, 1600–1606.
[61] Shannon, R. D. Revised effective ionic radii and systematic studies of interatomic distances in halides and chalcogenides. *Acta Cryst. Sect. A* **1976**, *32*, 751–767.
[62] Kahan, H. M.; Macfarlane, R. M. Optical and microwave spectra of Cr^{3+} in the Spinel $ZnGa_2O_4$. *J. Chem. Phys*. **1971**, *54*, 5197–5205.

[63] Dhak, P.; Gayen, U. K.; Mishra, S.; Pramanik, P.; Roy, A. Optical emission spectra of chromium doped nanocrystalline zinc gallate. *J. Appl. Phys.* **2009**, *106*, 063721.
[64] Zhou, Z. H.; Zheng, W.; Kong, J. T.; Liu, Y.; Huang, P.; Zhou, S. Y.; Chen, Z.; Shi, J. L.; Chen, X. Y. Rechargeable and LED-activated $ZnGa_2O_4$:Cr^{3+} near-infrared persistent luminescence nanoprobes for background-free biodetection. *Nanoscale* **2017**, *9*, 6846–6853.
[65] van Gorkom, G. G. P.; Henning, J. C. M.; van Stapele, R. P. Optical spectra of Cr^{3+} pairs in the spinel $ZnGa_2O_4$. *Phys. Rev. B* **1973**, *8*, 955–973.
[66] Dai, W. B.; Lei, Y. F.; Ye, S.; Song, E. H.; Chen, Z.; Zhang, Q. Y. Mesoporous nanoparticles Gd_2O_3@$mSiO_2$/$ZnGa_2O_4$: Cr^{3+}, Bi^{3+} as multifunctional probes for bioimaging. *J. Mater. Chem. B* **2016**, *4*, 1842–1852.
[67] Zou, R.; Huang, J. J.; Shi, J. P.; Huang, L.; Zhang, X. J.; Wong, K. L.; Zhang, H. W.; Jin, D. Y.; Wang, J.; Su, Q. Silica shell-assisted synthetic route for mono-disperse persistent nanophosphors with enhanced *in vivo* recharged near-infrared persistent luminescence. *Nano Res.* **2017**, *10*, 2070–2082.
[68] Srivastava, B. B.; Kuang, A.; Mao, Y. B. Persistent luminescent sub-10 nm Cr doped $ZnGa_2O_4$ nanoparticles by a biphasic synthesis route. *Chem. Commun.* **2015**, *51*, 7372–7375.
[69] Teston, E.; Richard, S.; Maldiney, T.; Lièvre, N.; Wang, G. Y.; Motte, L.; Richard, C.; Lalatonne, Y. Non-aqueous sol–gel synthesis of ultra small persistent luminescence nanoparticles for near-infrared *in vivo* imaging. *Chem.—Eur. J.* **2015**, *21*, 7350–7354.
[70] Fonger, W. H.; Struck, C. W. Temperature dependences of Cr^{3+} radiative and nonradiative transitions in ruby and emerald. *Phys. Rev. B* **1975**, *11*, 3251–3260.
[71] Yang, J.; Liu, Y. X.; Zhao, Y. Y.; Gong, Z.; Zhang, M.; Yan, D. T.; Zhu, H. C.; Liu, C. G.; Xu, C. S.; Zhang, H. Ratiometric afterglow nanothermometer for simultaneous *in situ* bioimaging and local tissue temperature sensing. *Chem. Mater.* **2017**, *29*, 8119–8131.
[72] Yan, W. Z.; Liu, F.; Lu, Y. Y.; Wang, X. J.; Yin, M.; Pan, Z. W. Near infrared long-persistent phosphorescence in $La_3Ga_5GeO_{14}$:Cr^{3+} phosphor. *Opt. Express* **2010**, *18*, 20215–20221.
[73] Pan, Z. W.; Lu, Y. Y.; Liu, F. Sunlight-activated long-persistent luminescence in the near-infrared from Cr^{3+}-doped zinc gallogermanates. *Nat. Mater.* **2011**, *11*, 58–63.
[74] Wang, J.; Ma, Q. Q.; Hu, X. X.; Liu, H. Y.; Zheng, W.; Chen, X. Y.; Yuan, Q.; Tan, W. H. Autofluorescence-free targeted tumor imaging based on luminous nanoparticles with composition-dependent size and persistent luminescence. *ACS Nano* **2017**, *11*, 8010–8017.
[75] Li, Y.; Zhou, S. F.; Li, Y. Y.; Sharafudeen, K.; Ma, Z. J.; Dong, G. P.; Peng, M. Y.; Qiu, J. R. Long persistent and photo-stimulated luminescence in Cr^{3+}-doped Zn–Ga–Sn–O phosphors for deep and reproducible tissue imaging. *J. Mater. Chem. C* **2014**, *2*, 2657–2663.
[76] Li, Y.; Li, Y. Y.; Chen, R. C.; Sharafudeen, K.; Zhou, S. F.; Gecevicius, M.; Wang, H. H.; Dong, G. P; Wu, Y. L; Qin, X. X. et al. Tailoring of the trap distribution and crystal field in Cr^{3+}-doped non-gallate phosphors with near-infrared long-persistence phosphorescence. *NPG Asia Mater.* **2015**, *7*, e180.
[77] Jin, Y. H.; Hu, Y. H.; Chen, L.; Ju, G. F.; Wu, H. Y.; Mu, Z. F.; He, M.; Xue, F. H. Luminescent properties of a green long persistent phosphor Li_2MgGeO_4:Mn^{2+}. *Opt. Mater. Express* **2016**, *6*, 929–937.
[78] Takahashi, Y.; Ando, M.; Ihara, R.; Fujiwara, T. Green-emissive Mn-activated nanocrystallized glass with willemite-type Zn_2GeO_4. *Opt. Mater. Express* **2011**, *1*, 372–378.
[79] Terraschke, H.; Wickleder, C. UV, blue, green, yellow, red, and small: Newest developments on Eu^{2+}-doped nanophosphors. *Chem. Rev.* **2015**, *115*, 11352–11378.
[80] Cheng, J. G.; Li, P. L.; Wang, Z. J.; Li, Z. L.; Tian, M. M.; Wang, C.; Yang, Z. P. Color selective manipulation in $Li_2ZnGe_3O_8$:Mn^{2+} by multiple-cation substitution on different crystal-sites. *Dalton Trans.* **2018**, *47*, 4293–4300.
[81] Maldiney, T.; Lecointre, A.; Viana, B.; Bessière, A.; Bessodes, M.; Gourier, D.; Richard, C.; Scherman, D. Controlling electron trap depth to enhance optical properties of persistent luminescence nanoparticles for *in vivo* imaging. *J. Am. Chem. Soc.* **2011**, *133*, 11810–11815.
[82] Wang, J.; Ma, Q. Q.; Zheng, W.; Liu, H. Y.; Yin, C. Q.; Wang, F. B.; Chen, X. Y.; Yuan, Q.; Tan, W. H. One-dimensional luminous nanorods featuring tunable persistent luminescence for autofluorescence-free biosensing. *ACS Nano* **2017**, *11*, 8185–8191.
[83] Li, Z. H.; Wang, Q.; Wang, Y. Q.; Ma, Q. Q.; Wang, J.; Li, Z. H.; Li, Y. X.; Lv, X. B.; Wei, W.; Chen, L. et al. Background-free latent fingerprint imaging based on nanocrystals with long-lived luminescence and pH-guided recognition. *Nano Res.* **2018**, *11*, 6167–6176.
[84] Che, G. B.; Liu, C. B.; Li, X. Y.; Xu, Z. L.; Liu, Y.; Wang, H. Luminescence properties of a new Mn^{2+}-activated red long-afterglow phosphor. *J. Phys. Chem. Solids* **2008**, *69*, 2091–2095.
[85] Li, P. F.; Peng, M. Y.; Wondraczek, L.; Zhao, Y. Q.; Viana, B. Red to near infrared ultralong lasting luminescence from Mn^{2+}-doped sodium gallium aluminum germanate glasses and (Al, Ga)-albite glass-ceramics. *J. Mater. Chem. C* **2015**, *3*, 3406–3415.
[86] Zhou, Z.; Zhou, N.; Xia, M.; Yokoyama, M.; Hintzen, H. T. Research progress and application prospects of transition metal Mn^{4+}-activated luminescent materials. *J. Mater. Chem. C* **2016**, *4*, 9143–9161.
[87] Adachi, S.; Takahashi, T. Photoluminescent properties of K_2GeF_6:Mn^{4+} red phosphor synthesized from aqueous HF/$KMnO_4$ solution. *J. Appl. Phys.* **2009**, *106*, 013516.
[88] Hiltunen, L.; Hölsä, J.; Strek, W.; Jezowska-Trzebiatowska, B. Crystal structure of $((C_4H_9)_4N)_3(Pr(NCS)_6)$. *J. Less-Common Met.* **1987**, *127*, 225–230.
[89] Jia, W.; Jia, D.; Rodriguez, T.; Evans, D. R.; Meltzer, R. S.; Yen, W. M. UV excitation and trapping centers in $CaTiO_3$:Pr^{3+}. *J. Lumin.* **2006**, *119–120*, 13–18.
[90] Yin, S. Y.; Chen, D. H.; Tang, W. J. Combustion synthesis and luminescent properties of $CaTiO_3$:Pr,Al persistent phosphors. *J. Alloys Compd.* **2007**, *441*, 327–331.
[91] Li, Y.; Li, Y. Y.; Sharafudeen, K.; Dong, G. P.; Zhou, S. F.; Ma, Z. J.; Peng, M. Y.; Qiu, J. R. A strategy for developing near infrared long-persistent phosphors: Taking $MAlO_3$:Mn^{4+},Ge^{4+} (M = La, Gd) as an example. *J. Mater. Chem. C* **2014**, *2*, 2019–2027.
[92] Du, J. R.; De Clercq, Q. O.; Korthout, K.; Poelman, D. $LaAlO_3$: Mn^{4+} as near-infrared emitting persistent luminescence phosphor for medical imaging: A charge compensation study. *Materials* **2017**, *10*, 1422.
[93] Zhang, X. W.; Nie, J. M.; Liu, S. S.; Li, Y.; Qiu, J. R. Deep-red photoluminescence and long persistent luminescence in double perovstkite-type La_2MgGeO_6:Mn^{4+}. *J. Am. Ceram. Soc.* **2018**, *101*, 1576–1584.
[94] Xue, F. H.; Hu, Y. H.; Chen, L.; Wu, H. Y.; Ju, G. F.; Wang, T.; Yang, L. A novel rare-earth free red long-persistent phosphor: Mg_2GeO_4:Mn^{4+}. *Ceram. Int.* **2017**, *43*, 15141–15145.
[95] Binnemans, K. Lanthanide-based luminescent hybrid materials. *Chem. Rev.* **2009**, *109*, 4283–4374.
[96] Bünzli, J. C. G. Benefiting from the unique properties of lanthanide ions. *Acc. Chem. Res.* **2006**, *39*, 53–61.
[97] Chen, G. Y.; Qiu, H. L.; Prasad, P. N.; Chen, X. Y. Upconversion nanoparticles: Design, nanochemistry, and applications in theranostics. *Chem. Rev.* **2014**, *114*, 5161–5214.
[98] Zhu, X. J.; Su, Q. Q.; Feng, W.; Li, F. Y. Anti-Stokes shift luminescent materials for bio-applications. *Chem. Soc. Rev.* **2017**, *46*, 1025–1039.
[99] Wang, F.; Liu, X. G. Multicolor tuning of lanthanide-doped nanoparticles by single wavelength excitation. *Acc. Chem. Res.* **2014**, *47*, 1378–1385.
[100] Liu, Y. S.; Tu, D. T.; Zhu, H. M.; Chen, X. Y. Lanthanide-doped luminescent nanoprobes: Controlled synthesis, optical spectroscopy, and bioapplications. *Chem. Soc. Rev.* **2013**, *42*, 6924–6958.
[101] Gai, S. L.; Li, C. X.; Yang, P. P.; Lin, J. Recent progress in rare earth micro/nanocrystals: Soft chemical synthesis, luminescent properties, and biomedical applications. *Chem. Rev.* **2014**, *114*, 2343–2389.
[102] Bünzli, J. C. G.; Eliseeva, S. V. Lanthanide NIR luminescence for telecommunications, bioanalyses and solar energy conversion. *J. Rare Earths* **2010**, *28*, 824–842.
[103] Bünzli, J. C. G.; Pecharsky V. K. *Handbook on the Physics and Chemistry of Rare Earths*; Elsevier: Oxford, 2013.
[104] Smet, P.; Avci, N.; Poelman, D. Red persistent luminescence in Ca_2SiS_4:Eu,Nd. *J. Electrochem. Soc.* **2009**, *156*, H243–H248.
[105] Liang, Y. J.; Liu, F.; Chen, Y. F.; Wang, X. L.; Sun, K. N.; Pan, Z. W. Red/near-infrared/short-wave infrared multi-band persistent luminescence in Pr^{3+}-doped persistent phosphors. *Dalton Trans.* **2017**, *46*, 11149–11153.
[106] Dai, W. B.; Lei, Y. F.; Zhou, J.; Xu, M.; Chu, L. L.; Li, L.; Zhao, P.; Zhang, Z. H. Near-infrared quantum-cutting and long-persistent phosphor $Ca_3Ga_2Ge_3O_{12}$:Pr^{3+},Yb^{3+} for application in *in vivo* bioimaging and dye-sensitized solar cells. *J. Alloys Compd.* **2017**, *726*, 230–239.
[107] Kamimura, S.; Xu, C. N.; Yamada, H.; Marriott, G.; Hyodo, K.; Ohno, T. Near-infrared luminescence from double-perovskite $Sr_3Sn_2O_7$:Nd^{3+}: A new class of probe for *in vivo* imaging in the second optical window of biological tissue. *J. Ceram. Soc. Jpn.* **2017**, *125*, 591–595.
[108] Liang, Y. J.; Liu, F.; Chen, Y. F.; Wang, X. J.; Sun, K. N.; Pan, Z. W. New

function of the Yb^{3+} ion as an efficient emitter of persistent luminescence in the short-wave infrared. *Light*: *Sci*. *Appl*. **2016**, *5*, e16124.
[109] Zou, Z. H.; Wu, C.; Li, X. D.; Zhang, J. C.; Li, H. H.; Wang, D. Y.; Wang, Y. H. Near-infrared persistent luminescence of Yb^{3+} in perovskite phosphor. *Opt*. *Lett*. **2017**, *42*, 4510–4512.
[110] Lv, Y.; Wang, L.; Zhuang, Y. X.; Zhou, T. L.; Xie, R. J. Discovery of the Yb^{2+}–Yb^{3+} couple as red-to-NIR persistent luminescence emitters in Yb-activated $(Ba_{1-x}Sr_x)AlSi_5O_2N_7$ phosphors. *J*. *Mater*. *Chem*. *C* **2017**, *5*, 7095–7101.
[111] Caratto, V.; Locardi, F.; Costa, G. A.; Masini, R.; Fasoli, M.; Panzeri, L.; Martini, M.; Bottinelli, E.; Gianotti, E.; Miletto, I. NIR persistent luminescence of lanthanide ion-doped rare-earth oxycarbonates: The effect of dopants. *ACS Appl*. *Mater*. *Interfaces* **2014**, *6*, 17346–17351.
[112] Gong, X. Y.; Cui, R. R.; Li, X. C.; Huang, W. C.; Deng, C. Y. The photoluminescence and afterglow properties of Ca_2SnO_4:Sm^{3+} phosphor. *J*. *Mater*. *Sci*.: *Mater*. *Electron*. **2018**, *29*, 5668–5674.
[113] Ju, G. F.; Hu, Y. H.; Chen, L.; Jin, Y. H.; Li, Y. Persistent luminescence in $BaGd_2O_4$:Dy^{3+}: From blue to infrared. *Appl*. *Phys*. *A* **2018**, *124*, 39.
[114] Chen, W. B.; Wang, Y. H.; Zeng, W.; Li, G.; Guo, H. J. Design, synthesis and characterization of near-infrared long persistent phosphors $Ca_4(PO_4)_2O$:Eu^{2+},R^{3+} (R = Lu, La, Gd, Ce, Tm, Y). *RSC Adv*. **2016**, *6*, 331–337.
[115] Zhang, X. M.; Zhang, J. H.; Zhang, X.; Chen, L.; Lu, S. Z.; Wang, X. J. Enhancement of red fluorescence and afterglow in $CaTiO_3$:Pr^{3+} by addition of Lu_2O_3. *J*. *Lumin*. **2007**, *122–123*, 958–960.
[116] Takasaki, H; Tanabe, S.; Hanada, T. Long-lasting afterglow characteristics of Eu, Dy codoped SrO-Al_2O_3 phosphor. *J*. *Ceram*. *Soc*. *Jpn*. **1996**, *104*, 322–326.
[117] Yu, N. Y.; Liu, F.; Li, X. F.; Pan, Z. W. Near infrared long-persistent phosphorescence in $SrAl_2O_4$:Eu^{2+},Dy^{3+},Er^{3+} phosphors based on persistent energy transfer. *Appl*. *Phys*. *Lett*. **2009**, *95*, 231110.
[118] Klink, S. I.; Grave, L.; Reinhoudt, D. N.; van Veggel, F. C. J. M.; Werts, M. H. V.; Geurts, F. A. J.; Hofstraat, J. W. A systematic study of the photophysical processes in polydentate triphenylene-functionalized Eu^{3+}, Tb^{3+}, Nd^{3+}, Yb^{3+}, and Er^{3+} complexes. *J*. *Phys*. *Chem*. *A* **2000**, *104*, 5457–5468.
[119] Vicentini, G; Zinner, L. B.; Zukerman-Schpector, J.; Zinner, K. Luminescence and structure of europium compounds. *Coord*. *Chem*. *Rev*. **2000**, *196*, 353–382.
[120] Adam, J. L.; Docq, A. D.; Lucas, J. Optical transitions of Dy^{3+} ions in fluorozirconate glass. *J*. *Solid State Chem*. **1988**, *75*, 403–412.
[121] Welsher, K.; Sherlock, S. P.; Dai, H. J. Deep-tissue anatomical imaging of mice using carbon nanotube fluorophores in the second near-infrared window. *Proc*. *Natl*. *Acad*. *Sci*. *USA* **2011**, *108*, 8943–8948.
[122] Hong, G. S.; Lee, J. C.; Robinson, J. T.; Raaz, U.; Xie, L. M.; Huang, N. F.; Cooke, J. P.; Dai, H. J. Multifunctional *in vivo* vascular imaging using near-infrared II fluorescence. *Nat*. *Med*. **2012**, *18*, 1841–1846.
[123] Dorenbos, P. Systematic behaviour in trivalent lanthanide charge transfer energies. *J*. *Phys*.: *Condens*. *Matter* **2003**, *15*, 8417–8434.
[124] Bos, A. J. J.; Dorenbos, P.; Bessière, A.; Viana, B. Lanthanide energy levels in YPO_4. *Radiat*. *Meas*. **2008**, *43*, 222–226.
[125] Lyu, T. S.; Dorenbos, P. Charge carrier trapping processes in lanthanide doped $LaPO_4$, $GdPO_4$, YPO_4, and $LuPO_4$. *J*. *Mater*. *Chem*. *C* **2018**, *6*, 369–379.
[126] Luo, H. D.; Bos, A. J. J.; Dorenbos, P. Controlled electron–hole trapping and detrapping process in $GdAlO_3$ by valence band engineering. *J*. *Phys*. *Chem*. *C* **2016**, *120*, 5916–5925.
[127] Xia, Z. G.; Li Q.; Sun J. Y. Greenish-yellow light-emitting, long-lasting phosphorescence in Eu^{2+}-doped CaO–$CaBr_2$–SiO_2 phosphor system. *Chem*. *Lett*. **2006**, *35*, 764–765.
[128] Dexter, D. L. A theory of sensitized luminescence in solids. *J*. *Chem*. *Phys*. **1953**, *21*, 836–850.
[129] Főrster T. 10th Spiers Memorial Lecture. Transfer mechanisms of electronic excitation. *Discuss*. *Faraday Soc*. **1959**, *27*, 7–17.
[130] Jinnai, K.; Kabe, R.; Adachi, C. Wide-range tuning and enhancement of organic long-persistent luminescence using emitter dopants. *Adv*. *Mater*. **2018**, *30*, 1800365.
[131] Zhu, C. L.; Liu, L. B.; Yang, Q.; Lv, F. T.; Wang, S. Water-soluble conjugated polymers for imaging, diagnosis, and therapy. *Chem*. *Rev*. **2012**, *112*, 4687–4735.
[132] Li, K.; Liu, B. Polymer-encapsulated organic nanoparticles for fluorescence and photoacoustic imaging. *Chem*. *Soc*. *Rev*. **2014**, *43*, 6570–6597.
[133] Wu, C. F.; Chiu, D. T. Highly fluorescent semiconducting polymer dots for biology and medicine. *Angew*. *Chem*., *Int*. *Ed*. **2013**, *52*, 3086–3109.
[134] Pu, K. Y.; Shuhendler, A. J.; Jokerst, J. V.; Mei, J. G.; Gambhir, S. S.; Bao, Z. N.; Rao, J. H. Semiconducting polymer nanoparticles as photoacoustic molecular imaging probes in living mice. *Nat*. *Nanotechnol*. **2014**, *9*, 233–239.
[135] Shuhendler, A. J.; Pu, K. Y.; Cui, L. N.; Uetrecht, J. P.; Rao, J. H. Real-time imaging of oxidative and nitrosative stress in the liver of live animals for drug-toxicity testing. *Nat*. *Biotechnol*. **2014**, *32*, 373–380.
[136] Pu, K. Y.; Shuhendler, A. J.; Rao, J. H. Semiconducting polymer nanoprobe for *in vivo* imaging of reactive oxygen and nitrogen species. *Angew*. *Chem*., *Int*. *Ed*. **2013**, *52*, 10325–10329.
[137] Palner, M.; Pu, K. Y.; Shao, S.; Rao, J. H. Semiconducting polymer nanoparticles with persistent near-infrared luminescence for *in vivo* optical imaging. *Angew*. *Chem*. **2015**, *127*, 11639–11642.
[138] Miao, Q. Q.; Xie, C.; Zhen, X.; Lyu, Y.; Duan, H, W.; Liu, X. G.; Jokerst, J. V.; Pu, K. Y. Molecular afterglow imaging with bright, biodegradable polymer nanoparticles. *Nat*. *Biotechnol*. **2017**, *35*, 1102–1110.
[139] Xie, C.; Zhen, X.; Miao, Q. Q.; Lyu, Y.; Pu, K. Y. Self-assembled semiconducting polymer nanoparticles for ultrasensitive near-infrared afterglow imaging of metastatic tumors. *Adv*. *Mater*. **2018**, *30*, 1801331.
[140] Katayama, Y.; Kayumi, T.; Ueda, J.; Tanabe, S. Enhanced persistent red luminescence in Mn^{2+}-doped (Mg, Zn)GeO_3 by electron trap and conduction band engineering. *Opt*. *Mater*. **2018**, *79*, 147–151.